

A model of thermodynamic stabilization of nanocrystalline grain boundaries in alloy systems

Omar Hussein and Yuri Mishin

June 11, 2024

Department of Physics and Astronomy, MSN 3F3, George Mason University, Fairfax, Virginia 22030, USA

Abstract

Nanocrystalline (NC) materials are intrinsically unstable against grain growth. Significant research efforts have been dedicated to suppressing the grain growth by solute segregation, including the pursuit of a special NC structure that minimizes the total free energy and completely eliminates the driving force for grain growth. This fully stabilized state has been predicted theoretically and by simulations but is yet to be confirmed experimentally. To better understand the nature of the full stabilization, we propose a simple two-dimensional model capturing the coupled processes of grain boundary (GB) migration and solute diffusion. Kinetic Monte Carlo simulations based on this model reproduce the fully stabilized polycrystalline state and link it to the condition of zero GB free energy. The simulations demonstrate the emergence of a fully stabilized state by the divergence of capillary wave amplitudes on planar GBs and by fragmentation of a large grain into a stable ensemble of smaller grains. The role of solute diffusion in the full stabilization is examined. Possible extensions of the model are discussed.

Keywords: Nanocrystal, alloy, grain boundary, thermodynamics, stability, Monte Carlo

1 Introduction

Many nanocrystalline (NC) materials exhibit physical and mechanical properties superior to those of coarse-grained materials. However, a major obstacle to broader applications of

NC materials is their instability against grain growth at elevated temperatures. The excess grain boundary (GB) free energy γ gives rise to capillary forces driving GB migration to reduce the GB area. The excess free energy in NC materials is extremely high, often making the grain growth virtually unstoppable. Significant research efforts have been dedicated to suppressing the grain growth by alloying the material with suitable solutes. Such solutes segregate to GBs and either lower their free energy or reduce their mobility (or both). Grain growth retardation by alloying has been achieved in numerous alloy systems. Unfortunately, the stabilization by alloying becomes less effective at high temperatures because GB segregation weakens while GB mobility increases. Another limiting factor is the competition between GB segregation and bulk phase transformations.

Three decades ago, Weissmuller [1, 2] suggested that, under certain conditions, the total free energy of a NC alloy can reach a minimum at a *finite* grain size. In this special state, the driving force for grain coarsening vanishes, and the material becomes thermodynamically stable against grain growth. We refer to this special state as *fully stabilized*. Thermodynamic analysis [3–17] confirmed the theoretical possibility of full stabilization. The conditions of full stabilization were investigated in great detail within the regular solution model [9–23], and the results were presented as stability diagrams convenient for alloys design. Metropolis Monte Carlo simulations [11, 16, 24] have demonstrated that, under certain combinations of the regular solution parameters, a polycrystal can reach equilibrium with a finite grain size, confirming the full stabilization. On the other hand, despite the abundant experimental evidence of grain growth inhibition by alloying, there is no convincing evidence that a fully stabilized NC state has been realized. Further theoretical and simulation efforts are required to better understand the nature of the full stabilization and assess the feasibility of its practical implementation.

The goal of this paper is to investigate two aspect of the NC stabilization problem. The first one is related to the conditions of full stabilization. Assuming that GB segregation is uniform across the entire GB area in the sample (which is a strong approximation), it can be shown (see Appendix) that reaching a total free energy minimum is equivalent to the condition of zero GB free energy (per unit area): $\gamma = 0$. To create this state, the system must be closed (no solute exchange with the environment) and have a nano-scale grain size, so that the solute storage capacities of the GBs and the grains would be comparable. In an open system, an initially planar GB must develop diverging capillary fluctuations as γ approaches zero. In a closed system, the capillary fluctuations must increase but remain finite. Once the fully stabilized state is reached, the $\gamma = 0$ condition can be verified by directly computing the GB free energy (e.g., by thermodynamic integration). To our knowledge, this type of analysis has not been carried out.

The second aspect is related to the role of solute diffusion in the NC stability. The previous theoretical analyses [1–23] had a *global* character. The free energy was minimized with respect to the total GB area (assumed to be proportional to the average grain size) under the constraints of GB-solute equilibrium and a fixed total amount of the solute. This constrained minimization tacitly assumes that local GB displacements are accompanied by instant redistribution of the solute across the entire system, quickly creating a new GB-solute equilibrium corresponding to the changed GB area. The Monte Carlo simulations [11, 16, 24] are similarly global: the solute and solvent atoms are randomly exchanged across the entire system, ensuring fast global re-equilibration in response to variations in the number of GB sites. The assumption of instant re-equilibration is incompatible with the finite rate of solute diffusion. The GB displacements are *local* events accompanied by absorption or rejection of some amount of the solute. Diffusion-controlled redistribution of this solute cannot be fast enough to immediately restore the GB-solute equilibrium everywhere in the sample. Equilibrium will be lost, at least locally and temporarily. It is unclear *a priori* whether the structure minimizing the total free energy with respect to variations in the total GB area will be stable against other variations, such as local perturbations of the grain size distribution. Answering this question requires a model explicitly treating both solute diffusion and GB migration.

In this paper, we develop a simple model of a polycrystalline alloy that captures solute diffusion and solute interactions with stationary and moving GBs. The model is more conceptual than quantitative. It is only intended to probe the fundamental aspects of the full GB stabilization mentioned above. It combines a two-dimensional (2D) Ising model on a square lattice with a solid solution model. Previous Monte Carlo simulations using the Ising or Potts models with solutes [11, 16, 25–28] employed the Metropolis algorithm. The latter is appropriate for equilibrium systems but does not predict the correct dynamics away from equilibrium. In particular, the Metropolis algorithm does not correctly describe diffusion in structurally inhomogeneous systems. To address this limitation, we develop a kinetic Monte Carlo (KMC) model describing concurrent operation of GB migration and solute diffusion. We apply this model to calculate the thermodynamic properties of alloy GBs, reproduce the fully stabilized polycrystalline state, verify the link between this state and the $\gamma = 0$ condition, and examine the role of solute diffusion in the full stabilization.

2 Model formulation

2.1 Structure and thermodynamics of the system

We consider a 2D array of square cells of size a arranged in a square pattern. The array is X cells long in the direction parallel to the Cartesian x -axis and Y cells long parallel to the Cartesian y -axis. Thus, the physical dimensions of the array are $aX \times aY$. The cells are enumerated by a single index $k = 1, 2, \dots, N$, where $N = XY$ is the total number of cells. Periodic boundary conditions are applied to mimic an infinitely large system.

The cells are interpreted as small crystalline blocks with two possible lattice orientations. We refer to these orientations as black and white and label them with a “spin” variable σ_k taking the values of $\sigma_k = 1$ and $\sigma_k = -1$ for the black and white orientations, respectively. The average orientation (color) of the system is characterized by the variable

$$I = \frac{\sum_k \sigma_k}{N}, \quad (1)$$

with $I = 1$ and $I = -1$ for the all-black and all-white single-crystalline states, respectively. Eq.(1) can also calculate the average color of a subset of cells.

In addition to the “spin” variable σ_k , we introduce another variable n_k defined as the number of unlike (opposite color) nearest neighbors of the cell k . The n_k values are related to the σ_k values by

$$n_k = 2 - \frac{\sigma_k}{2} \sum_{(kl)} \sigma_l, \quad (2)$$

where the symbol (kl) indicates summation over the four neighbors l of the cell k . If all neighbors have the same orientation as the cell k , then $n_k = 0$; if all neighbors have the opposite orientation, then $n_k = 4$. All other cases lie in between.

Next, we assume that unlike nearest-neighbor cells interact with a repulsive potential driving the system to a color separation. Specifically, each pair of nearest-neighbor cells with opposite orientation interacts with a positive energy $2J_{gg} > 0$, while nearest-neighbor pairs of the same orientation do not interact. Thus, for a given distribution of black and white cells, the crystallographic energy of the system is

$$E_{\text{cryst}} = \sum_k J_{gg} n_k. \quad (3)$$

Note that $E_{\text{cryst}} = 0$ in a single-crystalline state and reaches the maximum value of $E_{\text{cryst}} = 4J_{gg}N$ for a checkerboard arrangement of the cells.

This model is isomorphous to the 2D Ising model on a simple square lattice, in which the total energy is

$$E_{\text{Ising}} = -\frac{1}{2} \sum_{k,l} J \sigma_k \sigma_l - \sum_k h \sigma_k. \quad (4)$$

The interaction parameter J and the external field h are related to our model by $J = J_{gg}$ and $h = 0$. The average orientation I in Eq.(1) is similar to the magnetization in the Ising model.

If the system is partitioned into black and white domains, we interpret them as grains. Accordingly, boundaries between such domains, on which the crystallographic orientation switches from black to white, represent GBs. To track the motion of GBs, we introduce the GB locator function

$$\phi(n_k) = 1 - \frac{1}{4}(n_k - 2)^2 \quad (5)$$

representing the likelihood that a given cell k lies in a GB region. This function is zero inside a single crystal ($n_k = 0$) and for an isolated cell of opposite color relative to its environment ($n_k = 4$). Both cases are representative of a grain interior. The function reaches the maximum value of 1 for cells with $n_k = 2$. Such cells are transitional between the single-crystalline states on either side of the GB and can be associated with the GB region. Fig. 1(a) depicts a portion of a typical GB with the cells colored according to the n_k value. Note that the cells with $n_k = 2 \pm 1$ decorate the GB region, permitting its automated detection and tracking during simulations.

We next extend the model to include solute atoms, which can occupy some of the cells with one atom per cell. If the system contains $N_s \leq N$ solute atoms distributed among the cells, the average solute concentration is $c = N_s/N$. To model GB segregation, we assume that the GBs create a potential field attracting the solute atoms. To represent this field, the following term is added to the total energy:

$$E_{sg} = - \sum_k J_{sg} \xi_k \phi(n_k). \quad (6)$$

Here, ξ_k is a solute locator whose values are $\xi_k = 1$ if the cell k is occupied by a solute atom and $\xi_k = 0$ otherwise. Each term is multiplied by the GB locator $\phi(n_k)$, so the product $\xi_k \phi(n_k)$ identifies the GB cells occupied by solute atoms. The parameter $J_{sg} > 0$ controls the strength of GB segregation. Fig. 1(b) illustrates the solute attraction to the GB, with colors representing the values of $J_{sg} \xi_k \phi(n_k)$.

The model also includes interaction among the solute atoms. Only nearest-neighbor atoms are allowed to interact, and their interactions are assumed to be repulsive, driving the system to phase separation below a critical point. Furthermore, the solute-solute interactions generally differ inside the grains and in GBs. Given that the GBs are associated with $\phi(n_k)$ values close to 2, the strength of interactions must correlate with the function $\phi(n_k)$. Based on these considerations, we postulate the following form of the total energy

of solute-solute interactions:

$$E_{ss} = \frac{1}{2} \sum_k \xi_k \sum_{(kl)} \xi_l J_{ss} [1 + \eta \phi(n_{k,l})]. \quad (7)$$

In this equation, the solute locators ξ_k and ξ_l select nearest neighbor cells occupied by solute atoms, the factor of 1/2 eliminates the double-count of the atomic pairs, and we have introduced

$$n_{k,l} = \frac{n_k + n_l}{2} \quad (8)$$

as the average number of black-white bonds of the two solute atoms. The parameter $J_{ss} > 0$ is the strength of solute-solute interactions when both atoms are inside a grain, in which case $\phi(n_{k,l}) = 0$ and the term in the square brackets equals unity. If one or both atoms are in or near a GB, $\phi(n_{k,l})$ is positive and the interaction between the two atoms is modified, becoming stronger or weaker, depending on whether η is chosen positive or negative. If $n_k = n_l = 2$, the interaction parameter becomes $J_{ss} [1 + \eta]$. This setup allows us to control the solution thermodynamics in the grains and in the GB segregation atmosphere.

To summarize, the model describes a non-ideal solid solution in a polycrystalline structure with solute-GB interactions. Thermodynamic properties of the solution are different in the GBs and inside the grains. Each microstate of the system is defined by the set of parameters $\{\sigma_k, \xi_k\}$. The total energy of the system in a given microstate is

$$\begin{aligned} E &= E_{\text{cryst}} + E_{sg} + E_{ss} \\ &= \sum_k J_{gg} n_k - \sum_k J_{sg} \xi_k \phi(n_k) + \frac{1}{2} \sum_k \xi_k \sum_{(kl)} \xi_l J_{ss} [1 + \eta \phi(n_{k,l})]. \end{aligned} \quad (9)$$

The function $\phi(n_k)$ is defined by Eq.(5) and the numbers n_k and $n_{k,l}$ are given by Eqs.(2) and (8), respectively. The input material parameters of the model are J_{gg} , J_{sg} , J_{ss} , and η , which characterize the orientational interactions, the GB segregation energy, the solute-solute binding, and the GB thermodynamics, respectively.

2.2 Time evolution of the system

To model the dynamics of our system, we couple it to a thermostat at a temperature T and let it evolve by overcoming energy barriers between microstates by thermal fluctuations. Only transitions between microstates separated by a single energy maximum are considered. Furthermore, only two types of transition are allowed, which we call a flip and a jump. In a flip, a cell switches its color to the opposite one. Sequences of flips from black to white, or vice versa, can result in GB migration. In a jump event, a solute atom jumps to a nearest-neighbor cell. Such jumps constitute a mechanism of solute diffusion.

We adopt the harmonic transition state theory [29], by which the transition rate ν_{ij} from a microstate i to a microstate j is

$$\nu_{ij} = \nu_0 \exp\left(-\frac{\varepsilon_{ij}}{k_B T}\right), \quad (10)$$

where ε_{ij} is the transition barrier, k_B is Boltzmann's constant, and ν_0 is the attempt frequency. The latter is assumed to be the same for all transitions. The transition barrier ε_{ij} depends on the energy difference, $E_{ij} = E_j - E_i$, between the states i and j . If the system transitions to a lower-energy state ($E_j < E_i$), the barrier ε_{ij} must be lower than for the reverse transition (Fig. 2(a)). If the energy difference between the states is small, the linear approximation

$$\varepsilon_{ij} = \varepsilon_0 + E_{ij}/2 \quad (11)$$

is often used, in which ε_0 is the unbiased energy barrier (when $E_j = E_i$). The unbiased barriers are generally different for the flips and jumps; we denote them ε_0^g (flip) and ε_0^s (jump).

The linear approximation in Eq.(11) is only valid for weakly driven systems. This work adopts a more general, nonlinear model proposed in [30, 31]. In this model,

$$\varepsilon_{ij} = \begin{cases} \varepsilon_0 \exp\left(\frac{E_{ij}}{2\varepsilon_0}\right), & E_{ij} \leq 0, \\ E_{ij} + \varepsilon_0 \exp\left(-\frac{E_{ij}}{2\varepsilon_0}\right), & E_{ij} > 0. \end{cases} \quad (12)$$

If the energy difference E_{ij} is positive and large ($E_{ij} \gg \varepsilon_0$), the barrier is high and close to E_{ij} . If E_{ij} is negative and large in magnitude ($-E_{ij} \gg \varepsilon_0$), the barrier is exponentially small. In other words, a strong driving force suppresses the transition barrier but never makes it exactly zero. The barrier-energy relation within this model is illustrated in Fig. 2(b). Note that this relation guarantees the detailed balance of the forward and backward transitions.

It is known that GB diffusion is much faster than lattice diffusion and has a lower activation energy [32–34]. The effect is called “short circuit” diffusion and is observed in most (if not all) materials. To capture this effect, we make the unbiased barrier of solute diffusion different in GBs and inside the grains. To this end, we make ε_0^s a function of $\phi(n_{k,l})$. Namely, for a solute jump $k \rightarrow l$, the unbiased barrier is

$$\varepsilon_0^s = \varepsilon_{00}^s [1 - q\phi(n_{k,l})], \quad (13)$$

where ε_{00}^s is the barrier in a single crystal (for which $\phi(n_{k,l}) = 0$), and q is a parameter. The latter is adjusted to reduce the GB diffusion barrier. Indeed, in GB regions $\phi(n_{k,l}) \approx 1$

and thus $\varepsilon_0^s \approx \varepsilon_{00}^s [1 - q]$. Since ε_0^s cannot be negative, q must be smaller than 1. In this work, we take $q = 1/2$, which gives $\varepsilon_0^s \approx \varepsilon_{00}^s/2$ in reasonable agreement with experimental data [32–34]. Note that the environmental adjustment of the diffusion barriers only applies to solute atom jumps. The unbiased barrier of the flips (ε_0^g) remains constant.

3 Computer implementation of the model

In this section, we discuss the computer implementation of this model. The computations were performed in normalized variables whose relations to the physical variables are summarized in Table 1. All energies are normalized by J_{gg} , all distances by a , and the unit of time is the inverse attempt frequency, ν_0^{-1} . The normalized variables are denoted by the same symbols as the physical variables. This should not cause any confusion because we will only use the normalized variables from now on.

Two types of simulation were performed: simulations of equilibrium thermodynamic states of the system and simulations of the system dynamics. Accordingly, two different algorithms were used, as described below.

3.1 Thermodynamic property calculations

Equilibrium thermodynamic properties were calculated by Metropolis Monte Carlo simulations in the grand canonical ensemble. Starting from an initial state of the system, the simulations first brought the system to thermodynamic equilibrium, followed by a long production run to average the properties of interest.

Two types of trial moves were implemented: a flip and insertion or removal of a solute atom. At each Monte Carlo step, one of the two types of move was selected with equal probability (except for the solute-free simulations when only flips were considered). For a flip, the color of a randomly selected cell was reversed, and the energy change E_{ij} was calculated. The attempt was accepted with the probability

$$p_{ij} = \min \left(1, e^{-\frac{E_{ij}}{T}} \right). \quad (14)$$

For the solute insertion/removal, the occupation number ξ_k of a randomly selected cell k was switched to the opposite, and the attempt was accepted with the probability

$$p_{ij} = \min \left(1, e^{-\frac{E_{ij} \pm \mu}{T}} \right), \quad (15)$$

where μ is a preset value of the chemical potential. The sign in the exponent depends on whether the solute atom was removed (+) or inserted (-). Note that the flip case can

be formally considered as insertion/removal of a black cell with $\mu = 0$, so the statistical ensemble is grand-canonical in both cases. For both types of trial move, if p_{ij} was found to be < 1 , the acceptance decision was made by generating a random number $r \in (0, 1]$. The move was accepted if $p_{ij} \geq r$.

The equilibrium values of properties of interest were obtained by simple averaging over the visited microstates. We emphasize that the simulation implements a single trajectory in the configuration space $\{\sigma_k, \xi_k\}$. To ensure ergodicity of the sampling, the simulation must be repeated multiple times from random initial states.

3.2 Simulation of system dynamics

The system evolution was studied using KMC simulations. The system was coupled to a thermostat and chemically isolated while allowing non-conservative changes in the cell orientations. In other words, the statistical ensemble was canonical for solute jumps and grand-canonical with $\mu = 0$ for cell orientations. This allowed us to model the concurrent processes of solute diffusion and grain evolution.

A rejection-free KMC algorithm was implemented, which was similar to the n -way algorithm [35]. The simulations comprised the following steps:

1. Initialize the simulation: set the clock to zero ($t_0 = 0$), set the iteration number to zero ($m = 0$), and choose an initial microstate $i = \{\sigma_k, \xi_k\}$.
2. Use Eqs. (10) and (12) to calculate the set of rates $\{\nu_{ij}^s\}$ for all possible jumps of all solute atoms. Note that jumps to occupied cells are excluded from the calculation.
3. Calculate the total solute jump rate from the microstate i ,

$$R_i^s = \sum_{j=1}^{M_i^s} \nu_{ij}^s,$$

and the commutative jump probabilities

$$P_n^s = \frac{1}{R_i^s} \sum_{j=1}^n \nu_{ij}^s, \quad n = 1, 2, \dots, M_i^s.$$

Here, M_i^s is the total number of allowed solute jumps from the microstate i .

4. Perform similar calculations for the total flip rate R_i^f and the cumulative transition probabilities P_n^f ($n = 1, 2, \dots, N$) for all flips from the microstate i . The required flip rates $\{\nu_{ij}^f\}$ are obtained by flipping each cell, computing the energy change E_{ij} , and using Eqs. (10) and (12).

- Find the expected times to escape from the microstate i by making a solute jump (τ_i^s) and by a flip (τ_i^f). To this end, generate two random numbers $r_1, r_2 \in (0, 1]$ and calculate

$$\tau_i^s = -\frac{1}{R_i^s} \ln r_1, \quad \tau_i^f = -\frac{1}{R_i^f} \ln r_2.$$

- If $\tau_i^s < \tau_i^f$, implement a solute jump. To choose which atom will jump, draw a third random number $r_3 \in (0, 1]$ and find index n such that $P_{n-1}^s < r_3 \leq P_n^s$ (assuming $P_0^s = 0$). Execute the solute jump n by updating the respective occupation numbers. If $\tau_i^s \geq \tau_i^f$, implement a flip of the cell n such that $P_{n-1}^f < r_3 \leq P_n^f$ (assuming $P_0^f = 0$). Execute the flip by updating σ_n and recomputing the n_k and $n_{k,l}$ values for the cells affected by the flip.
- Update the iteration number to $m + 1$.
- Advance the clock: $t_m = t_{m-1} + \tau_m$, where $\tau_m = \min(\tau_i^s, \tau_i^f)$.
- Rename the new microstate to i .
- Return to step 3.

We emphasize that the KMC simulations are more suitable for modeling solute diffusion and GB migration than the Metropolis algorithm. The latter correctly describes the system in thermodynamic equilibrium and drives a non-equilibrium system towards equilibrium. However, the path towards the equilibrium state is not guaranteed to be physically meaningful. When making the accept/reject decisions, the Metropolis algorithm only considers the energies of the microstates and disregards the unbiased transition barriers. Specifically, the transition barrier to a higher-energy microstate is assumed to be equal to the energy difference between the microstates, while transitions to lower-energy microstates are barrier-free. This behavior is shown schematically in Fig. 2(b). In reality, the transition probabilities from a given microstate depend not only on the energies of the available destination microstates but also on the barriers separating those microstates from the current one. For example, if two destination microstates have the same energy but one is separated from the current microstate by a lower barrier, transition to the latter microstate is more probable. The higher probability of lower-barrier states with the same energy is built into the KMC algorithm proposed here. By contrast, the Metropolis algorithm will treat both transitions as equally probable. Due to this difference, the chains of transitions generated by the two algorithms are generally different.

The KMC algorithm can also be applied to sample equilibrium states and should give the same results as the Metropolis algorithm. Once an equilibrium state is reached, the

expected value of any property $\mathcal{P}(\{\sigma_k, \xi_k\})$ can be obtained by averaging along a long KMC trajectory:

$$\langle \mathcal{P} \rangle = \frac{\sum_{m=1}^K \tau_m \mathcal{P}_m}{\sum_{m=1}^K \tau_m}, \quad (16)$$

where \mathcal{P}_m is the value of the property in the microstate visited at the Monte Carlo step m , and $K \gg 1$ is the number of Monte Carlo steps on the trajectory. Assuming ergodicity, $\langle \mathcal{P} \rangle$ approximates the ensemble average of the property.

4 Equilibrium properties of the solute-free system

Before analyzing the GB-solute interactions, we applied the KMC algorithm to study the equilibrium properties of a solute-free system. The goal was threefold: (1) validate our methodology, (2) calculate the equilibrium properties of solute-free GBs for the subsequent comparison with those in the alloy system, and (3) generate reference data required for thermodynamic integration in the alloy systems. In the absence of solute atoms, the KMC simulations only implemented the flip transitions.

4.1 The bulk transition temperature

The bulk transition temperature was computed by a set of KMC simulations on a 128×128 system at temperatures T ranging from 0.1 to 10 with 0.1 increments. At each temperature, the simulation started with a single crystalline state and was run for about 10^7 Monte Carlo steps after the system reached equilibrium. The average color of the system is plotted as a function of temperature in Fig. 3(a). The heat capacity per atom, C , was calculated using two methods. First, the total energy $\langle E \rangle$ was computed from Eq.(16) as a function of T , and the heat capacity was obtained by numerical differentiation:

$$C = \frac{d \langle E \rangle}{dT}. \quad (17)$$

The second method was based on the fluctuation formula [36, 37]

$$C = \frac{\langle E^2 \rangle - \langle E \rangle^2}{T^2}. \quad (18)$$

As shown in Fig. 3(b,c), both methods give similar results, confirming the robustness of our algorithm. The heat capacity peak corresponds to the bulk phase transition, which allows us to estimate the transition temperature T_c at 2.28. For comparison, in the 2D

Ising model on a square lattice, the exact transition temperature derived by Onsager [38] is

$$T_c = \frac{2}{\ln(1 + \sqrt{2})} \approx 2.269. \quad (19)$$

The slight discrepancy could be reduced using a larger system and more temperatures, which we did not pursue.

At high temperatures approaching T_c from below, the initial grain ($I = \pm 1$) develops a high concentration of randomly distributed cells of opposite color. At the bulk transition temperature, the system becomes a random mixture of black and white cells in equal proportion ($I \rightarrow 0$). As shown in Fig. 3(a), the simulation results closely follow the analytical solution [39]

$$I = \left[1 - \operatorname{csch}^2 \left(\frac{2}{T} \right) \right]^{1/8}. \quad (20)$$

In magnetic systems, T_c represents the paramagnetic transition temperature. Given our interpretation of the cells as representing local lattice orientations, we can interpret T_c as the “melting” temperature of the single crystal. Note that a polycrystalline structure with equal numbers of black and white cells can also give $I = 0$ at temperatures below T_c . However, this structure is thermodynamically unstable: solute-free GBs in this model possess a positive excess free energy, which creates a driving force for grain coarsening. The coarsening continues until the system transforms into a single crystal with $I = \pm 1$. As shown later, solute atoms can stabilize GBs and create thermodynamically equilibrium polycrystalline structures below T_c .

4.2 GB free energy from thermodynamic integration

Thermodynamic properties of solute-free GBs were studied using a system of two GBs parallel to the x -axis. The system size in the direction normal to the GBs was fixed at $Y = 256$. Three system sizes parallel to the GBs were tested, with the X values of 128, 256, and 512. To ensure that the system has reached thermodynamic equilibrium and collect sufficient statistics of capillary waves, the simulations comprised about 10^9 Monte Carlo steps.

The interfacial free energy γ was calculated by the thermodynamic integration method reviewed by Binder et al. [40]. The method is based on the interfacial form of the Gibbs-Helmholtz equation,

$$\frac{\partial(\tilde{F}/T)}{\partial T} = -\frac{\tilde{E}}{T^2}, \quad (21)$$

where \tilde{E} and \tilde{F} are the excess GB energy and free energy, respectively. For a 2D system

with periodic boundaries,

$$\tilde{F} = \gamma L - TS, \quad (22)$$

where L is the GB length. The latter generally differs from its geometric length X due to the capillary waves. In Eq.(22), S is the configurational entropy of the GB, which takes into account that the GB can be located at any position along the y -axis without changing the system energy. For a single GB, $S = \ln Y$. Since we have two GBs, their configurational entropy is $S = \ln(Y^2/2)$, where we assumed that the GBs can choose their positions independently but swapping their positions does not create a new state (hence the division by 2). Thus, the configuration entropy per one GB is

$$S = \frac{1}{2} \ln \left(\frac{Y^2}{2} \right). \quad (23)$$

Eq.(21) is integrated with respect to temperature from a chosen reference temperature T_0 to the current temperature T :

$$\gamma = \gamma_0 \frac{XT}{LT_0} - \frac{T}{L} \int_{T_0}^T \frac{\tilde{E}}{T'^2} dT' + \frac{T}{L} \left[\ln \left(\frac{Y}{\sqrt{2}} \right) - S_0 \right], \quad (24)$$

where γ_0 is the GB free energy at the temperature T_0 . The reference temperature is chosen low enough to disregard the entropy effects and treat the GB as perfectly straight ($L = X$). At this temperature, we can take $\gamma_0 X = \tilde{E}_0$ and neglect the configurational entropy S_0 .

The excess energy \tilde{E} was calculated as follows:

$$\tilde{E} = \frac{1}{2} \left\langle E - \frac{Y}{Y_g} E_g \right\rangle. \quad (25)$$

The angular brackets denote the time averaging as in Eq.(16), and the factor of 1/2 is due to the presence of two GBs in the system. In Eq.(25), E is the total energy of the system and E_g is the energy of a single-crystalline region unaffected by the GBs. This region was chosen inside one of the grains with dimensions $X \times Y_g$ (Fig. 4).

We chose $T_0 = 0.3$, computed $\tilde{E}(T)$ on a temperature grid, and performed a quadratic spline interpolation for numerical integration. The GB free energy obtained is plotted as a function of temperature in Fig. 5(a). The curve agrees well with previous Metropolis Monte Carlo calculations within the Ising model [40]. In particular, the GB free energy decreases with temperature and converges to zero at the bulk critical temperature T_c . At this temperature, the difference between the grain orientation vanishes, and the GB ceases to exist.

4.3 GB stiffness calculation

In the previous section, the GB free energy was calculated for the GB orientation parallel to the x -axis. However, GB properties in this model are anisotropic. This anisotropy can be approximately represented by the GB stiffness α defined by

$$\alpha = \gamma_{||} + (\partial^2 \gamma / \partial \theta^2)_{||}, \quad (26)$$

where θ is the inclination angle of the GB relative to the x -axis. The symbol $||$ indicates that both γ and its second angular derivative refer to the $\theta \rightarrow 0$ limit.

We have computed the GB stiffness as a function of temperature by the capillary fluctuation method [41–44]. In this method, the fluctuated GB shape is decomposed into a Fourier series with amplitudes A_n . The mean-square Fourier amplitude is related to the GB stiffness by the equation (rewritten in our dimensionless variables)

$$\langle |A_n|^2 \rangle = \frac{T}{\alpha X k_n^2}, \quad (27)$$

where $k_n = (2\pi/X)n$ ($n = \pm 1, \pm 2, \dots$) are wave numbers. Thus, α can be extracted from the slope of the plot $\langle |A_n|^2 \rangle^{-1}$ versus k_n^2 in the long-wave (small k) limit.

The critical step in the capillary fluctuation method is to extract the GB shape from the simulation snapshots. The challenge is caused by the fuzziness of the GBs and the background noise in the grains. In our case, the grains contain numerous cells of the opposite color, either isolated or aggregated into small clusters reflecting the short-range order (Fig. 6(a)). This background noise was especially significant at high temperatures. An algorithm was developed to identify the “wrong” color cells/clusters lying outside the GBs and reverse their color to that of the grain (Fig. 6(b)). This grain-cleaning procedure was applied to all snapshots saved during the simulations. Next, the GBs were smoothed by a Gaussian filter whose width was adjusted to preserve the GB shape on a length scale moderately exceeding the cell size (Fig. 6(c)). Finally, the smoothed GB shape was traced ensuring a one-to-one correspondence (Fig. 6(d)).

The discrete Fourier transformation was applied to the smoothed GBs, and the Fourier amplitudes obtained were averaged over a set of KMC snapshots. The α values extracted from the $\langle |A_n|^2 \rangle^{-1}$ versus k_n^2 plots are shown in Fig. 3 as a function of temperature. The results agree well with previous Metropolis Monte Carlo simulation within the Ising model [40]. Like the GB free energy γ , the stiffness converges to zero at the bulk critical temperature T_c . At lower temperatures, the stiffness deviates from γ , indicating that the torque term in Eq.(26) becomes significant.

Note that α diverges to infinity at $T \rightarrow 0$. In this limit, the GB is nearly straight with a small concentration of kinks [45–47]. This GB structure creates a cusp in the angular

dependence of γ with a diverging second derivative. Although these calculations validate our methodology, the applicability of the capillary fluctuation method at low temperatures is questionable because the capillary wave amplitudes become indistinguishable from the intrinsic GB width. The difference between the intrinsic and capillary GB widths is discussed next.

4.4 One GB, two widths

A GB can be characterized by two widths, which differ both conceptually and numerically (Fig. 7(a)). The intrinsic GB width w_I is the width of the atomic-scale transition layer between the grains. The capillary GB width characterizes the amplitude of the capillary waves on a larger length scale. It is customary to quantify the capillary width by the mean-squared deviation $\langle w^2 \rangle$ from the average GB plane (line in 2D):

$$\langle w^2 \rangle \equiv \frac{1}{X} \left\langle \sum_{n=1}^X (y_n - \bar{y})^2 \right\rangle. \quad (28)$$

Here, y_n are y -coordinates of the GB cells and

$$\bar{y} = \frac{1}{X} \sum_{n=1}^X y_n$$

is the instantaneous GB position.

Both w_I and $\langle w^2 \rangle$ increase with temperature and diverge to infinity at the bulk critical point. At a given temperature, w_I and $\langle w^2 \rangle$ follow different system size dependencies. w_I is an intensive GB property and does not depend on the system size. By contrast, $\langle w^2 \rangle$ increases with the GB length X . Indeed, according to the capillary wave theory [30, 45–47],

$$\langle w^2 \rangle = \frac{TX}{12\alpha}. \quad (29)$$

This equation predicts a linear scaling with X .

In the simulations, $\langle w^2 \rangle$ could be readily calculated from the GB shapes discussed in the previous section. To calculate w_I , we developed a procedure illustrated in Fig. 7(b). The system was divided into thin slices parallel to the y -axis. The x -dimension of each slice was $\zeta \ll X$, so the GB portion within each slice could be treated as linear (no capillary waves). We found that $\zeta = 4$ was a reasonable choice. Each slice was further divided into thin layers parallel to the x -axis, and the color I of each layer was computed by averaging the σ -numbers of the cells using Eq.(1). This calculation produced a function $I(y)$ for each slice. This function was relatively close to 1 or -1 within the grains and transitioned

between these values across the GBs. In the transition region, this function was fitted by the hyperbolic tangent with three fitting parameters I_0 , y_0 (the local GB position), and w_I ,

$$I(y) = I_0 \tanh\left(\frac{y - y_0}{w_I}\right), \quad (30)$$

by minimizing the mean-squared deviation. The final result for w_I was obtained by averaging over the two GBs, all slices, and all snapshots saved during the simulations.

Fig. 5(b,c) shows the obtained temperature dependencies of w_I and $\langle w^2 \rangle$. As expected, both widths increase with temperature, reflecting the GB broadening as the average grain orientations (colors) converge at high temperatures. Note that the temperature dependencies of $\langle w^2 \rangle$ are fairly linear for all three system sizes tested, as predicted by Eq.(29). This equation also predicts that the plots for different system sizes must collapse into a single straight line when plotted in the $\langle w^2 \rangle / X$ versus T format. Fig. 5(d) shows that this prediction is borne out by the simulations. The remaining scatter is due to the statistical fluctuations increasing with temperature. Comparison of Fig. 5(b) and (c) indicates that the capillary GB width $\sqrt{\langle w^2 \rangle}$ is significantly larger than the intrinsic width w_I at $T > 0.5$, justifying the validity of the capillary fluctuation method at these temperatures.

5 Bulk thermodynamics of alloys

Having tested the thermodynamic properties of the solute-free system, we are now ready to investigate the alloy systems. Two computational methods will be applied. To study the equilibrium thermodynamics, we use the Metropolis Monte Carlo method described in section 3.1. We consider a 256×128 system connected to a thermostat at a temperature T and to an imaginary reservoir of solute atoms at a chemical potential μ . Upon equilibration, the system reaches a solute concentration c and an average orientation (color) I . Different equilibrium states can be explored by varying the control parameters T and μ . The results can be represented by phase diagrams in the coordinates T , c and I (note, however, that only two of them are independent variables). Having the phase diagrams, we then apply KMC simulations for a more detailed investigation of the equilibrium structures at different locations on the phase diagram. The KMC barriers $\varepsilon_0 = 1$, $\varepsilon_{00}^s = 1$, and $q = 0$ are chosen, but this choice does not play a role because we are only interested in equilibrium structures. The choice of the barriers will become important when we examine the role of solute diffusion in Section 7.

Different choices are possible for the solute-GB interaction energy J_{sg} and the solute-solute interaction energy J_{ss} . If the latter is positive, the alloy can separate into two

phases with different solute concentrations below a critical point that is different from the orientational critical temperature T_c . To simplify the parametric analysis, we will focus on the case of $J_{ss} = 0$. Accordingly, only variations in J_{sg} are considered.

We will assume that $J_{sg} > 0$ to ensure attraction between solute atoms and cells with mixed (black and white) environments. This attraction causes solute segregation to GBs, but it also produces the reverse effect, in which the solute atoms inside the grains tend to surround themselves with cells of opposite color relative to the color of the grain. In other words, the solute atoms amplify short-range disorder by promoting the formation of clusters of misoriented cells centered at a solute atom. The enhanced disorder can be expected to reduce the bulk critical point relative to the solute-free case. The misoriented cells surrounding a solute atom can be interpreted as lattice distortions existing around solute atoms in real crystals.

The surface plot in Fig. 8(a) is the $T - c - I$ phase diagram computed with $J_{sg} = 2$ (recall that J_{sg} is normalized by J_{gg}). The surface is colored according to temperature, and the lines on the surface are $c - I$ isotherms. In the $c \rightarrow 0$ limit, the ends of each isotherm converge to crystalline states with I values close to 1 or -1 . As the solute concentration increases at a fixed temperature, the positive and negative I values decrease in magnitude, indicating that the grains develop significant orientational disorder (as predicted above). At a critical solute concentration, both I values converge to zero, and the system becomes orientationally disordered. At this chemical composition, the chosen temperature becomes the critical temperature above which a crystalline state cannot exist.

The $I - T$ plot in Fig. 8(b) represents a set of iso-concentration cross-sections of the phase diagram. The $c = 0$ cross-section reproduces the solute-free diagram shown in Fig. 3(a). When the solute concentration becomes high enough, the iso-concentration cross-sections form closed loops. Such loops indicate that single crystalline states of the alloy only exist in a certain temperature interval. In other words, the alloy system has *two* critical points. The upper critical temperature smoothly connects to the solute-free T_c in the $c \rightarrow 0$ limit and represents a melting transition. The lower critical point exists only in alloys and represents a phenomenon in which a single crystal loses thermodynamic stability upon cooling below this temperature.

The existence of the low critical temperature is also evident from the nose-like shape of the surface in Fig. 8(a), in which the states under the nose (shown in blue) represent the low critical points. To further clarify the meaning of such points, we plot the critical temperature as a function of alloy composition in Fig. 9. This plot is the intersection of the phase diagram in Fig. 8(a) with the $I = 0$ plane. It shows that the critical temperature is a two-valued function of the chemical composition, with the upper and lower branches

representing two critical lines. The upper branch reflects the effect of critical point suppression by alloying mentioned above. The lower branch is the boundary of single-crystal stability at low temperatures. Single-crystalline states of either orientation only exist in the gray area on the left of the critical curve.

The insets in Fig. 9 display representative structures of the system in several parts of the phase diagram. These structures were obtained by closing the system (no solute exchange with the reservoir) and equilibrating it by KMC simulations. The images on the left show the structures of a white grain at the temperatures of 0.3, 0.9, and 1.5 with the fixed chemical composition of $c = 0.05$. Note the local disorder in the form of single and clustered black cells, which increases with temperature and becomes especially visible at $T = 1.5$.

The images on the right correspond to the same three temperatures but with a solute concentration of $c = 0.25$. At $T = 0.9$, the system is on the left of the critical line, so the single-crystalline state is stable. Compared to the $c = 0.05$ structure at the same temperature, more extensive clustering is observed due to the solute effect. At $T = 1.5$, single-crystalline states are unstable and the system is orientationally disordered with $I = 0$. Because this liquid-like state is relatively close to the critical line, it exhibits large orientational fluctuations on the scale comparable to the system size. Significant clustering into black and white regions is observed, in contrast to the homogeneous supercritical structure in the solute-free system (cf. Fig. 3(a)). Such regions are dynamic: they constantly form, dissolve, and move around while preserving the zero average orientation of the system ($I = 0$). Finally, the structure equilibrated at $T = 0.3$ is composed of black and white grains separated by sharp GBs with significant solute segregation. Note that the GBs are faceted, confirming that the structure is crystalline in contrast to the liquid-like state at $T = 1.5$. We interpret this structure as a thermodynamically stable polycrystalline state discussed in section 1. Since our model only considers two crystallographic orientations, the large GB area is achieved by forming enclosed grains, with black grains nested inside the white and vice versa.

To further demonstrate the different equilibrium states mentioned above, we created a circular black grain inside a white parent grain, as shown in Fig. 10. In the initial state, a uniform random distribution of solute atoms with $c = 0.25$ was created. The system was then equilibrated by KMC simulations at the temperatures of 0.3, 0.9, and 1.5. The initial, intermediate, and equilibrated structures obtained are shown in three columns. At $T = 1.5$, the black grain disintegrates, forming a disordered, liquid-like structure similar to that in Fig. 9. This behavior confirms that a crystalline state is unstable at this temperature. At $T = 0.9$, the crystalline state is expected to be stable according to the phase diagram. And

indeed, both grains remain crystalline but the black grain shrinks and soon disappears. This scenario indicates that the GB free energy is positive, creating a capillary driving force causing the grain shrinkage. Finally, at $T = 0.3$, the black grain does not shrink. Instead, it breaks into fragments and eventually forms a fine-grained structure with faceted GBs similar to the structure observed in Fig. 9. The fragmentation process increases the total GB area until the system arrives at thermodynamic equilibrium with a finite average grain size. In this structure, the GB free energy is expected to be zero.

The results shown above were obtained with the segregation energy of $J_{sg} = 2$. The effect of this energy on the phase diagram is illustrated in Fig. 11. At larger J_{sg} values, the nose shape of the critical line leading to the formation of stable polycrystals continues to exist. Furthermore, the polycrystalline state can be stabilized at smaller solute concentrations. As J_{sg} decreases, the critical line shifts towards higher concentrations and straightens until the GB stabilization effect disappears. In the $J_{sg} \rightarrow 0$ limit, polycrystalline states are less stable than a single crystal for any concentration, including the pure-solute system ($c = 1$).

6 Grain boundary free energy in alloys

To validate the link between the $\gamma = 0$ condition and the polycrystalline stability established in the previous section, we performed direct calculations of the GB free energy. The starting point was the 2D form of the Gibbs adsorption equation

$$d(\gamma L) = -\tilde{N}d\mu, \quad T = \text{const}, \quad (31)$$

where \tilde{N} is the total amount of GB segregation. The latter is defined by

$$\tilde{N} = (c - c_g)N/2, \quad (32)$$

where c_g is the solute concentration in grain regions unperturbed by the GBs, and c is the average solute concentration in the system. As before, the factor of two accounts for the presence of two GBs.

Integrating Eq.(31), we obtain

$$\gamma(T, \mu) = \frac{1}{L(T, \mu)} \left[\gamma(T, \mu_*)L(T, \mu_*) - \int_{\mu_*}^{\mu} \tilde{N}(T, \mu')d\mu' \right]. \quad (33)$$

We display all variables involved in the integration for the sake of clarity. The asterisk subscript refers to the reference state (T, μ_*) . Recall that L is the ensemble-averaged

GB length, which can differ from the system size X due to capillary fluctuations. In practice, the reference chemical potential μ_* is chosen to achieve the smallest possible solute concentration at which \tilde{N} can still be reliably extracted from the simulations. Then $\gamma(T, \mu_*)$ and $L(T, \mu_*)$ are approximated by their solute-free values at the temperature T . The solute-free $\gamma(T)$ values were calculated in section 4.2 by thermodynamic integration with respect to temperature. Technical details of computing the ensemble-averaged values of \tilde{N} and L and performing the numerical integration are presented in the online Supplementary Information file accompanying this article.

Metropolis Monte Carlo simulations were performed on a 128×256 system with two GBs parallel to the x -axis. Temperature was varied between 0.3 and 2.0, and the GB free energy $\gamma(T, \mu)$ was calculated from Eq.(33) at each temperature. The results were converted to the function $\gamma(T, c)$ using the relationship between μ and c known from the simulations.

Fig. 12(a) presents a three-dimensional surface plot of the function $\gamma(T, c)$ computed for $J_{sg} = 2$. The $c = 0$ cross-section of the surface is the solute-free GB free energy $\gamma(T)$ reported in section 4.2. The surface crosses the $\gamma = 0$ plane along the curve (shown in black) that matches the T versus c phase diagram in Fig. 9. Recall that this curve represents the boundary of single-crystalline stability. Beyond this boundary, single-crystalline alloys must transform into a liquid-like state or a stable polycrystal. The observed close agreement between the two independent calculations confirms the link between the polycrystal stabilization and the $\gamma = 0$ condition.

The γ versus c plots in Fig. 12(b) are isothermal cross-sections of the surface diagram in Fig. 12(a). At a fixed temperature, the GB free energy monotonically decreases with solute concentration, as predicted by the adsorption equation in Eq.(31) considering that $d\mu/dc > 0$. Fig. 12(c) shows the temperature dependencies of γ at fixed alloy compositions. The plots reveal a competition between the GB disordering and GB segregation. In dilute alloys, γ monotonically decreases with temperature due to the structural disordering of GBs at high temperatures, which increases the GB excess entropy. This trend is typical of elemental GBs and is followed by the present model, see Fig. 5(a). As the solute concentration increases, the curves turn over at low temperatures. This reversal is due to the increase in GB segregation at low temperatures. The segregation causes a decrease in γ , which eventually overpowers the disordering effect.

7 Solute segregation and grain boundary morphology

In this section, we perform a more detailed investigation of GB segregation and GB morphology as a function of alloy composition, temperature, and the segregation energy J_{sg} . We use the KMC algorithm because our goal is to study GBs in contact with nanoscale grains in a closed system, in which the solute supply to the GBs is controlled by diffusion. When we are only interested in equilibrium properties, we implement fast diffusion conditions to accelerate the approach to equilibrium. As before, we consider two GBs parallel to the x -axis with fully periodic boundary conditions. The GBs are characterized by the excess segregation \tilde{N} , intrinsic width w_I , and the mean-square capillary width w^2 . \tilde{N} was computed as discussed in section 6, and the GB widths were calculated by the same method as in the solute-free system (section 4.4).

In Fig. 13(a), we plot the equilibrium amount of solute segregation \tilde{N} as a function of temperature for the average solute concentration $c = 0.01$. (The results for higher concentrations are similar except that all \tilde{N} values are larger.) The system size is 128×256 , and the calculations have been performed for several values of J_{sg} . Each curve ends when the GB disintegrates transforming into a liquid-like state. The plots show that the segregation is high at low temperatures and decreases with temperature. This trend is typical for alloys with a positive segregation energy. As J_{sg} increases, the curves shift upward due to the stronger segregation.

In Fig. 13(b), we plot the equilibrium intrinsic GB width w_I and the capillary width $w_c \equiv \sqrt{w^2}$ as a function of temperature for several J_{sg} values. The plots show that both widths increase with temperature due to the thermal fluctuations and partial GB disordering. In the alloy, both widths are systematically larger than in the solute-free system ($J_{sg} = 0$). At a fixed temperature, both widths increase with J_{sg} . In other words, segregation thickness GBs and increases the amplitude of capillary waves. Fig. 13(c) shows the GB morphologies at three representative points labeled c1, c2, and c3. At the lowest-temperature point c1, the GBs are nearly saturated with the solute (explaining the large \tilde{N} value) and display a high degree of unevenness with some amount of faceting. At a lower temperature (point c2), more solute is distributed inside the grains at the expense of GBs (smaller \tilde{N}), and the faceting nearly vanishes. At the high temperature approaching the bulk critical point (c3), the solute atoms are scattered nearly uniformly. The grains are significantly disordered and contain a distribution of small clusters of the opposite orientation.

Note that at $J_{sg} \geq 4$, the capillary width exhibits a minimum and increases with decreasing temperature at low temperatures. This behavior can be attributed to a decrease in the GB stiffness caused by the solute segregation. Recall that in section 4.3, we were able

to extract the GB stiffness of solute-free GBs from the capillary fluctuation amplitudes. It would be tempting to apply the capillary fluctuation method to quantify the GB stiffness in the alloys. However, as discussed in Refs. [30, 31], Eqs.(27) and (29) cannot be applied to alloys, except in the limiting cases of exceedingly fast or exceedingly slow solute diffusion. Nevertheless, the predicted inverse correlation between the capillary wave amplitudes and GB stiffness remains qualitatively valid. We can, thus, infer from Fig. 13(b) that GB segregation reduces the GB stiffness, and that the extent of this reduction increases with decreasing temperature.

To further demonstrate the link between GB segregation and capillary fluctuations, we studied a set of closed systems with the same size $X = 128$ parallel to the GBs and four different sizes $Y = 64, 128, 256,$ and 512 in the normal direction. Initially, the solute atoms were distributed uniformly across the system with a concentration of $c = 0.1$. KMC simulations were run at the temperature of $T = 0.7$. During the simulations, the atoms diffused towards the GBs and formed segregation atmospheres. Since the total amount of solute in the system increased with the size Y , more solute was available to form the GB segregation. The limit of $Y \rightarrow \infty$ would create the open-system condition, but for the finite Y values tested here, the system remained closed. The GB images in Figure 14(a) show that the amount of segregation and the capillary wave amplitude both increase as the grain size increases. This correlation is quantified in Figure 14(b) showing that the capillary GB width increases monotonically with the system size. The rate of increase depends on the segregation energy J_{sg} , with higher J_{sg} values leading to larger capillary wave amplitudes for the same system size.

Finally, we return to the role of finite solute diffusion rates in the full stabilization. To demonstrate this role, we have created a circular grain similar to the one discussed previously (cf. Fig. 10), except that the simulation parameters are now $T = 0.7$, $c = 0.05$, and $J_{sg} = 7$. This situation represents a GB that broke away from its segregation atmosphere and found itself inside a grain. Two diffusion regimes will be considered. First, when the solute diffusion barrier is low ($\varepsilon_{00}^s = 1$) and thus diffusion is fast, the solute quickly catches up with the GB's new position and forms a new segregation atmosphere (Fig. 15). The GB free energy falls below zero and the grain starts increasing its area by breaking into smaller grains. The grain refinement process continues until the $\gamma = 0$ condition is met and the system reaches equilibrium. This process is illustrated in Fig. 15(a). The fraction of GB sites f is plotted as a function of time in Fig. 15(b), demonstrating that the system has reached equilibrium. This scenario is consistent with the previous theoretical analyses and Metropolis Monte Carlo simulations effectively implementing the fast diffusion conditions. In the the second regime, the diffusion barrier is higher ($\varepsilon_{00}^s = 25$) and the solute

diffusion is much slower. Since the initial GB free energy is positive, the grain shrinks and soon disappears on a time scale much shorter than the time scale of diffusion. Fig. 15(b) shows that f quickly drops to the background level (f includes not only the actual GBs but also the clusters of misoriented cells inside the grains, which the algorithm treats as tiny “grains”). Once the grain is gone, it is highly unlikely that new grains can nucleate homogeneously even if the simulation is run long enough to allow significant diffusion. The system will remain single-crystalline and with a higher free energy than the fully equilibrated polycrystal. This example shows that changes in the solute diffusion rate can lead to different stable or metastable states starting from the same initial structure, chemical composition, and temperature.

8 Concluding remarks

The model proposed here describes GB migration coupled to solute diffusion. The grain orientations are represented by a 2D Ising model, and the solute atoms diffuse by nearest-neighbor jumps with environmentally-dependent barriers. Despite its simplicity, the model captures a variety of physical effects, including GB disordering at high temperatures, GB segregation of the solute atoms, solute-solute interactions (which can be different in GBs and inside the grains), and accelerated solute diffusion along GBs relative to the grains. One of the limitations of the model is that it only represents two possible lattice orientations. As a result, polycrystalline structures are composed of hierarchically enclosed grains, with one enclosed grain enclosing another, and so on. As such, the model cannot represent triple junctions of grains, which are typical structural elements in polycrystalline materials. In addition, the underlying square lattice creates strongly anisotropic GB properties and leads to GB faceting at low temperatures. In the future, the model can be extended to higher-symmetry lattices (such as the hexagonal lattice) to reduce the anisotropy and include several lattice orientations using a Potts model. Extension to 3D polycrystals should also be possible.

Based on this model, we developed a rejection-free KMC algorithm implementing the two concurrent processes: lattice reorientations and solute atom jumps. This KMC algorithm distinguishes our work from previous simulations, which implemented an Ising or Potts model with solutes using a Metropolis Monte Carlo algorithm with unconditional acceptance of trial moves when $E_{ij} \leq 0$ [25–28, 48]. In addition to simulating unphysical dynamics, many implementations of the Metropolis algorithm had a global character. The swaps of randomly selected pairs of atoms, which can be far apart, can effectively sample the configuration space of an equilibrium system or rapidly drive the system towards equi-

librium. However, non-equilibrium processes, such as diffusion-controlled redistribution of solute atoms, occur unrealistically fast. The proposed KMC algorithm correctly represents solute diffusion as a random walk by nearest-neighbor jumps with adjustable jump barriers. Such barriers are coupled to the lattice orientations, allowing us to control diffusion rates in the perfect lattice and in defected regions such as GBs.

The model reproduces the fully stabilized polycrystalline state at relatively low temperatures in a certain range of segregation energies and solute concentrations. If solute diffusion is sufficiently fast, the alloy transforms into a fully stabilized polycrystal by breaking the initial large grain into fragments, each representing a new grain. Alternatively, an initially planar GB can develop large capillary waves before breaking into smaller grains. In reality, there could be other grain refinement mechanisms not captured by this model.

The solute diffusion rate plays a significant role in the formation of fully stabilized structures. The present model suggests that slow solute diffusion can reroute the system evolution into non-equilibrium or metastable states, and might possibly prevent the full stabilization. The question of whether the full stabilization observed (under certain conditions) in this model will be confirmed by more realistic models with multiple lattice orientations is left for future research.

Appendix: derivation of the $\gamma = 0$ condition

In this Appendix, we provide a rigorous derivation of the $\gamma = 0$ condition of full stability of a polycrystalline alloy. Although the derivation is based on Gibbs' interface thermodynamics, Gibbs treated bulk phases as infinite reservoirs of the chemical components and heat. Here, we apply Gibbs' method to a finite-size system. Also, while Gibbs derived all equations starting from the fundamental equation in the energy-entropy representation, we simplify the derivation by using the free energy. This implies that we assume uniform temperature across the system.

Consider an m -component polycrystalline alloy in internal thermodynamic equilibrium, thermal equilibrium with a thermostat at a temperature T , and mechanical equilibrium with a barostat at a pressure p . The system is closed (no matter exchange with the environment) and contains N_i ($i = 1, 2, \dots, m$) atoms of each chemical species. The system volume is V .

We assume that intensive properties of the solid solution inside the grains are uniform and the same in all grains. We further adopt the uniform boundary model, in which all grain boundaries (GBs) are characterized by the same properties. Following Gibbs' interface thermodynamics [49], we mentally partition the polycrystal into a grain system

and a GB system. The grain system is an imaginary uniform solid solution filling the volume V and having the same intensive properties as the grain interiors. For example, if the number density of atoms i inside the grains is n_i , then the grain system contains a total of $N_i^g = n_i V$ atoms of the component i .

The fundamental equation describing the grain system is its free energy F^g expressed as a function of T , V , and the numbers of atoms N_i^g :

$$F^g = F^g(T, V, N_1^g, N_2^g, \dots, N_m^g). \quad (34)$$

The remaining free energy, \tilde{F} , is attributed to the GB system and is called the total GB excess free energy. Thus, the total free energy of the polycrystal, F , is partitioned into F^g and \tilde{F} :

$$F = F^g + \tilde{F}. \quad (35)$$

Similarly, we introduce excesses of all other extensive properties. For example, the excess amounts of the chemical components are $\tilde{N}_i = N_i - N_i^g$, the excess GB entropy is $\tilde{S} = S - S^g$ (where $S^g = -\partial F^g / \partial T$), etc.

The central postulate of the interface thermodynamics is that the interfaces (in this case, GBs) follow their own fundamental equation in the form

$$\tilde{F} = \tilde{F}(T, A, \tilde{N}_1, \tilde{N}_2, \dots, \tilde{N}_m), \quad (36)$$

where A is the total GB area. In other words, the GB system can be treated as 2D phase on par with the 3D (bulk) phase forming the grains [50]. Although the two phases have a different dimensionality, they are described by mathematically similar fundamental equations. The only difference is that the volume V of the bulk phase is replaced by the area A (2D “volume”) of GBs. It follows that all thermodynamic equations describing a bulk phase can be immediately rewritten for the GB phase by merely changing the notations.

The grain free energy F^g in Eq.(34) is a homogeneous first degree function of the variables V and all N_i^g . By Euler’s theorem,

$$F^g = -pV + \sum_i \mu_i N_i^g, \quad (37)$$

where $\mu_i = \partial F^g / \partial N_i^g$ are the chemical potentials in the grains and we used the mechanical equilibrium condition

$$p = -\frac{\partial F^g}{\partial V}. \quad (38)$$

Taking the differential of F^g , we have

$$dF^g = -S^g dT - p dV + \sum_i \mu_i dN_i^g. \quad (39)$$

Combining Eqs.(37) and (39), we obtain the Gibbs-Duhem equation

$$-S^g dT + V dp - \sum_i N_i^g d\mu_i = 0. \quad (40)$$

We can now write down similar equations for the GB system:

$$\tilde{F} = \frac{\partial \tilde{F}}{\partial A} A + \sum_i \frac{\partial \tilde{F}}{\partial \tilde{N}_i} \tilde{N}_i, \quad (41)$$

$$d\tilde{F} = \frac{\partial \tilde{F}}{\partial T} dT + \frac{\partial \tilde{F}}{\partial A} dA + \sum_i \frac{\partial \tilde{F}}{\partial \tilde{N}_i} d\tilde{N}_i, \quad (42)$$

$$\frac{\partial \tilde{F}}{\partial T} dT - Ad \left(\frac{\partial \tilde{F}}{\partial A} \right) - \sum_i \tilde{N}_i d \left(\frac{\partial \tilde{F}}{\partial \tilde{N}_i} \right) = 0. \quad (43)$$

In a closed system, the mass conservation constraint dictates $d\tilde{N}_i + dN_i^g = 0$ for every species i . Also, we define

$$\gamma = \frac{\partial \tilde{F}}{\partial A} \quad (44)$$

and call it the GB free energy or GB tension. This quantity is a 2D analog of the 3D pressure p (compare with Eq.(38)). As a result, the above equations take the form

$$\tilde{F} = \gamma A + \sum_i \frac{\partial \tilde{F}}{\partial \tilde{N}_i} \tilde{N}_i, \quad (45)$$

$$d\tilde{F} = -\tilde{S} dT + \gamma dA - \sum_i \frac{\partial \tilde{F}}{\partial \tilde{N}_i} dN_i^g, \quad (46)$$

$$-\tilde{S} dT - Ad\gamma - \sum_i \tilde{N}_i d \left(\frac{\partial \tilde{F}}{\partial \tilde{N}_i} \right) = 0. \quad (47)$$

Next, we will need the total free energy F and its differential dF . These are readily obtained by adding the respective equations from above:

$$F = F^g + \tilde{F} = -pV + \gamma A + \sum_i \mu_i N_i^g + \sum_i \frac{\partial \tilde{F}}{\partial \tilde{N}_i} \tilde{N}_i, \quad (48)$$

$$dF = dF^g + d\tilde{F} = -SdT - pdV + \gamma dA + \sum_i \left(\mu_i - \frac{\partial \tilde{F}}{\partial \tilde{N}_i} \right) dN_i^g. \quad (49)$$

We can now formulate the conditions of chemical equilibrium between the GBs and the grains. Suppose T , V , and A are fixed, and an infinitesimal amount dN_i^g of atoms i moves from the GBs into the grains. The first-order variation of the total free energy with respect

to this variation must be zero. It follows that the last term in Eq.(49) must be identically zero. Thus, the GB-grain equilibrium condition is

$$\frac{\partial \tilde{F}}{\partial \tilde{N}_i} = \mu_i \quad (50)$$

for every species i . Inserting this condition into Eqs.(48) and (49), we finally obtain

$$F = -pV + \gamma A + \sum_i \mu_i N_i, \quad (51)$$

$$dF = -SdT - pdV + \gamma dA. \quad (52)$$

We emphasize that Eq.(52) represents equilibrium variations maintaining the GB-grain equilibrium.

Eq.(52) is what we wanted to derive. It shows that

$$\left(\frac{\partial F}{\partial A} \right)_{T,V} = \gamma. \quad (53)$$

If $\gamma > 0$, the free energy increases with GB area. In other words, to decrease the free energy, the grains must grow. If $\gamma < 0$, the polycrystal will tend to decrease the grain size (increase A). To obtain a stable polycrystal with a finite grain size, γ must change sign as shown schematically in Fig. 16. The free energy minimum is reached at $\gamma = 0$.

Although Eqs.(51) and (52) look similar to the known equations from Gibbs [49], they have been derived for a finite-size closed system, and their meaning is subtly different. To appreciate the difference, recall that the GB free energy is commonly defined as the reversible work of creating a unit GB area in a closed system. This definition implies GB creation in an initially single-crystalline system having the same temperature and volume and containing the same number of atoms of every species as the polycrystal. This definition appears to be consistent with Eq.(51), which can be rewritten in the form

$$\gamma = \frac{F - (\sum_i \mu_i N_i - pV)}{A}, \quad (54)$$

where the term in the parentheses is the free energy of a uniform solid solution. However, this is *not* the free energy of the imaginary solution that initially filled the volume V and from which the polycrystal has been formed. That solution follows the same fundamental equation (34) as the grains but with a different chemical composition:

$$F^0 = F^g(T, V, N_1, N_2, \dots, N_m) = -p^0V + \sum_i \mu_i^0 N_i. \quad (55)$$

The chemical potentials in that solution, $\mu_i^0 = \partial F^g / N_i$, are different from those in the grains due to the GB segregation. The pressure p^0 is generally also different. The free energy change relative that original solution is

$$F - F^0 = \gamma A - (p - p^0)V + \sum_i (\mu_i - \mu_i^0) N_i. \quad (56)$$

Eq.(56) shows that γA is generally different from the free energy change $F - F^0$ relative to the original solution. The difference arises because additional free energy is expended to change the chemical composition of the uniform solid solution. The GBs only know the chemical composition in the adjacent grains, and this is what defines γ . The grain composition only represents the composition of the original solution if the grains are large enough or the system is open. In that case, $\mu_i \rightarrow \mu_i^0$, $p \rightarrow p^0$, and we recover the known relation

$$\gamma = \frac{F - F^0}{A}. \quad (57)$$

References

- [1] J. Weissmüller, Alloy thermodynamics in nano-structures, *J. Mater. Res.* 9 (1994) 4–7.
- [2] J. Weissmüller, Alloy effects in nanostructures, *Nanostructured Materials* 3 (1993) 261–272.
- [3] R. Kirchheim, Grain coarsening inhibited by solute segregation, *Acta Materialia* 50 (2002) 413–419.
- [4] F. Liu, R. Kirchheim, Nano-scale grain growth inhibited by reducing grain boundary energy through solute segregation, *Journal of Crystal Growth* 264 (2004) 385–391.
- [5] R. Kirchheim, Reducing grain boundary, dislocation line and vacancy formation energies by solute segregation. I. Theoretical background, *Acta Mater.* 55 (2007) 5129–5138.
- [6] R. Kirchheim, Reducing grain boundary, dislocation line and vacancy formation energies by solute segregation. II. Experimental evidence and consequences, *Acta Mater.* 55 (2007) 5139–5148.
- [7] C. E. Krill, H. Ehrhardt, R. Birringer, Thermodynamic stabilization of nanocrystallinity, *International Journal of Materials Research* 96 (2005) 1134–1141.

- [8] L. S. Schvindlerman, G. Gottstein, Unexplored topics and potentials of grain boundary engineering, *Scripta Mater.* 54 (2006) 1041–1045.
- [9] A. J. Detor, C. A. Schuh, Grain boundary segregation, chemical ordering and stability of nanocrystalline alloys: Atomistic computer simulations in the ni-w system, *Acta Mater.* 55 (2007) 4221–4232.
- [10] T. Chookajorn, H. A. Murdoch, C. A. Schuh, Design of stable nano-crystalline alloys, *Science* 337 (2012) 951–953.
- [11] T. Chookajorn, C. A. Schuh, Thermodynamics of stable nanocrystalline alloys: A Monte Carlo analysis, *Phys. Rev. B* 89 (2014) 064102.
- [12] A. R. Kalidindi, C. A. Schuh, Stability criteria for nanocrystalline alloys, *Acta Mater.* 132 (2017) 128–137.
- [13] T. C. A. R. Kalidindi, C. A. Schuh, Nanocrystalline materials at equilibrium: A thermodynamic review, *JOM* 67 (2015) 2834–2843.
- [14] A. R. Kalidindi, C. A. Schuh, Stability criteria for nanocrystalline alloys, *J. Mater. Res.* 32 (2017) 1093–2002.
- [15] H. A. Murdoch, C. A. Schuh, Stability of binary nanocrystalline alloys against grain growth and phase separation, *Acta Mater.* 61 (2013) 2121–2132.
- [16] J. R. Trelewicz, C. A. Schuh, Grain boundary segregation and thermodynamically stable binary nanocrystalline alloys, *Phys. Rev. B* 79 (2009) 094112.
- [17] A. E. Perrin, C. A. Schuh, Stabilized nanocrystalline alloys: The intersection of grain boundary segregation with processing science, *Annual Review of Materials Research* 51 (2021) 241–268.
- [18] C. C. Koch, R. O. Scattergood, K. A. Darling, J. E. Semones, Stabilization of nanocrystalline grain sizes by solute additions, *J. Mater. Sci.* 43 (2008) 7264–7272.
- [19] K. A. Darling, M. A. Tschopp, B. K. VanLeeuwen, M. A. Atwater, Z. K. Liu, Mitigating grain growth in binary nanocrystalline alloys through solute selection based on thermodynamic stability maps, *Comp. Mater. Sci.* 84 (2014) 255–266.
- [20] M. Saber, H. Kotan, C. C. Koch, R. O. Scattergood, Thermodynamic stabilization of nanocrystalline binary alloys, *J. Appl. Phys.* 113 (2013) 065515.

- [21] M. Saber, H. Kotan, C. C. Koch, R. O. Scattergood, A predictive model for thermodynamic stability of grain size in nanocrystalline ternary alloys, *J. Appl. Phys.* 114 (2013) 103510.
- [22] W. Xing, A. R. Kalidindi, D. Amram, C. A. Schuh, Solute interaction effects on grain boundary segregation in ternary alloys, *Acta Materialia* 161 (2018) 285–294.
- [23] N. Zhou, J. Luo, Developing thermodynamic stability diagrams for equilibrium-grain-size binary alloys, *Materials Letters* 115 (2014) 268–271.
- [24] A. R. Kalidindi, T. Chookajorn, C. A. Schuh, Nanocrystalline materials at equilibrium: A thermodynamic review, *JOM* 67 (2015) 2834–2843.
- [25] M. I. Mendeleev, D. J. Srolovitz, W. E, Grain-boundary migration in the presence of diffusing impurities: simulations and analytical models, *Philos. Mag.* 81 (2001) 2243–2269.
- [26] M. I. Mendeleev, D. J. Srolovitz, Kink model for extended defect migration in the presence of diffusing impurities: theory and simulation, *Acta Materialia* 49 (2001) 2843–2852.
- [27] J. M. Liu, Monte carlo simulation of solute aggregation on domain boundaries in binary alloys: Domain-boundary segregation and domain growth, *Physical Review B* 58 (1998) 633–640.
- [28] J. M. Liu, L. C. Lim, Z. G. Liu, Monte carlo simulation of solute aggregation in binary alloys: Domain boundary precipitation and domain growth, *Physical Review B* 60 (1999) 7113–7126.
- [29] G. H. Vineyard, Frequency factors and isotope effects in solid state rate processes, *Journal of Physics and Chemistry of Solids* 3 (1957) 121–127.
- [30] Y. Mishin, Stochastic model and kinetic monte carlo simulation of solute interactions with stationary and moving grain boundaries. ii. application to two-dimensional systems, *Physical Review Materials* 7 (2023) 063404.
- [31] Y. Mishin, Stochastic model and kinetic monte carlo simulation of solute interactions with stationary and moving grain boundaries. i. model formulation and application to one-dimensional systems, *Physical Review Materials* 7 (2023) 063403.
- [32] I. Kaur, Y. Mishin, W. Gust, *Fundamentals of Grain and Interphase Boundary Diffusion*, Wiley, Chichester, West Sussex, 1995.

- [33] Y. Mishin, C. Herzig, J. Bernardini, W. Gust, Grain boundary diffusion: fundamentals to recent developments, *Int. Mater. Reviews* 42 (1997) 155.
- [34] Y. Mishin, C. Herzig, Grain boundary diffusion: recent progress and future research, *Mater. Sci. Eng. A* 260 (1999) 55–71.
- [35] A. B. Bortz, M. H. Kalos, J. L. Lebowitz, A new algorithm for monte carlo simulation of ising spin systems, *Journal of Computational Physics* 17 (1975) 10–18.
- [36] L. D. Landau, E. M. Lifshitz, Statistical Physics, Part I, volume 5 of *Course of Theoretical Physics*, third ed., Butterworth-Heinemann, Oxford, 2000.
- [37] Y. Mishin, Thermodynamic theory of equilibrium fluctuations, *Annals of Physics* 363 (2015) 48–97.
- [38] L. Onsager, Crystal statistics. i. a two-dimensional model with an order-disorder transition, *Physical Review* 65 (1944) 117–149.
- [39] C. N. Yang, The spontaneous magnetization of a two-dimensional ising model, *Physical Review* 85 (1952) 808–816.
- [40] K. Binder, B. Block, S. K. Das, P. Virnau, D. Winter, Monte carlo methods for estimating interfacial free energies and line tensions, *J. Statist. Phys.* 144 (2011) 690–729.
- [41] J. J. Hoyt, M. Asta, A. Karma, Method for computing the anisotropy of the solid-liquid interfacial free energy, *Phys. Rev. Lett.* 86 (2001) 5530–5533.
- [42] J. Morris, X. Song, The melting lines of model systems calculated from coexistence simulations, *J. Chem. Phys.* 116 (2002) 9352–9358.
- [43] G. P. P. Pun, V. Yamakov, J. Hickman, E. H. Glaessgen, Y. Mishin, Development of a general-purpose machine-learning interatomic potential for aluminum by the physically informed neural network method, *Physical Review Materials* 4 (2020) 113807.
- [44] Y. Mishin, Calculation of the γ/γ' interface free energy in the Ni-Al system by the capillary fluctuation method, *Modeling Simul. Mater. Sci. Eng.* 22 (2014) 045001.
- [45] M. P. Gelfand, M. E. Fisher, Finite-size effects in fluid interfaces, *Physica A: Statistical Mechanics and its Applications* 166 (1990) 1–74.
- [46] J. Lapujoulade, The roughening of metal surfaces, *Surface Science Reports* 20 (1994) 195–249.

- [47] Y. Saito, *Statistical Physics of Crystal Growth*, World Scientific, Singapore, 1996.
URL: <https://doi.org/10.1142/3261>. doi:doi:10.1142/3261.
- [48] M. I. Mendelev, D. J. Srolovitz, Domain wall migration in 3-d in the presence of diffusing impurities, *Interface Science* 10 (2002) 243–250.
- [49] J. W. Gibbs, *The collected works of J. W. Gibbs, volume 1*, Yale University Press, New Haven, 1948.
- [50] T. Frolov, Y. Mishin, Phases, phase equilibria, and phase rules in low-dimensional systems, *J. Chem. Phys.* 143 (2015) 044706.

Table 1: Table of physical and normalized variables in this model.

Variable	Physical	Normalized
System dimensions	Xa, Ya	X, Y
Temperature	T	$k_B T / J_{gg}$
Total energy	E	E / J_{gg}
Heat capacity	C	C / k_B
Solute–interface interaction energy	J_{sg}	J_{sg} / J_{gg}
Solutes interaction energy	J_{ss}	J_{ss} / J_{gg}
Time	t	$t\nu_0$
GB energy	γ	$\gamma a / J_{gg}$
GB stiffness	α	$\alpha a / J_{gg}$
GB length	L	$L / (Xa)$
Wave number	k_n	$k_n a$
Fourier amplitude	A_n	A_n / a
Mean squared GB width	w^2	w^2 / a^2
Intrinsic GB width	w_I	w_I / a
Chemical potential	μ	μ / J_{gg}

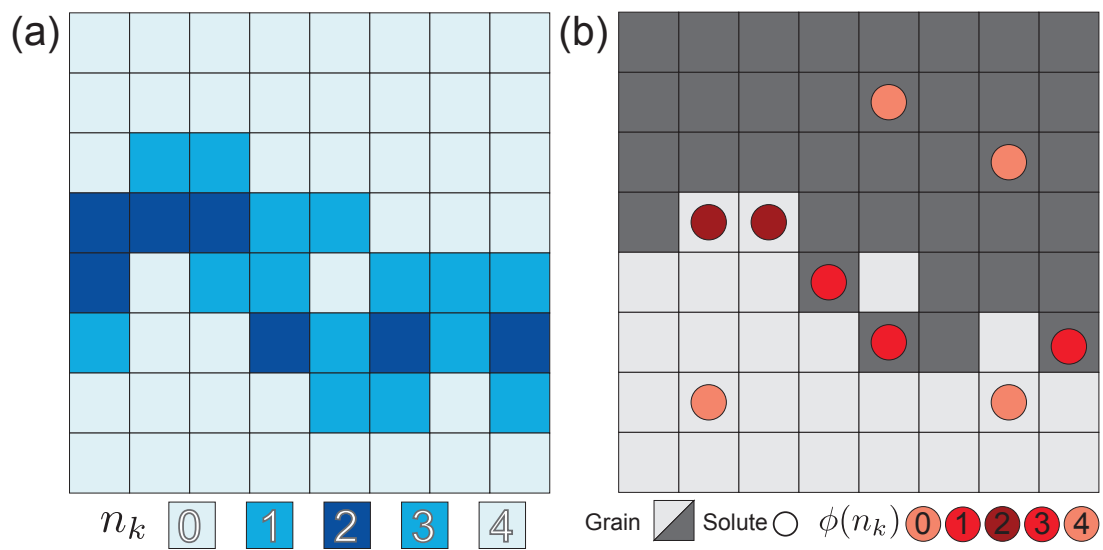


Figure 1: Schematic presentation of a typical grain boundary in the present model. (a) Color-coded values of the parameter n_k showing the concentration of cells with $n_k = 2 \pm 1$ in the GB region. (b) Typical distribution of solute atoms color-coded by the parameter $\phi(n_k)$, demonstrating solute attraction to the GB region.

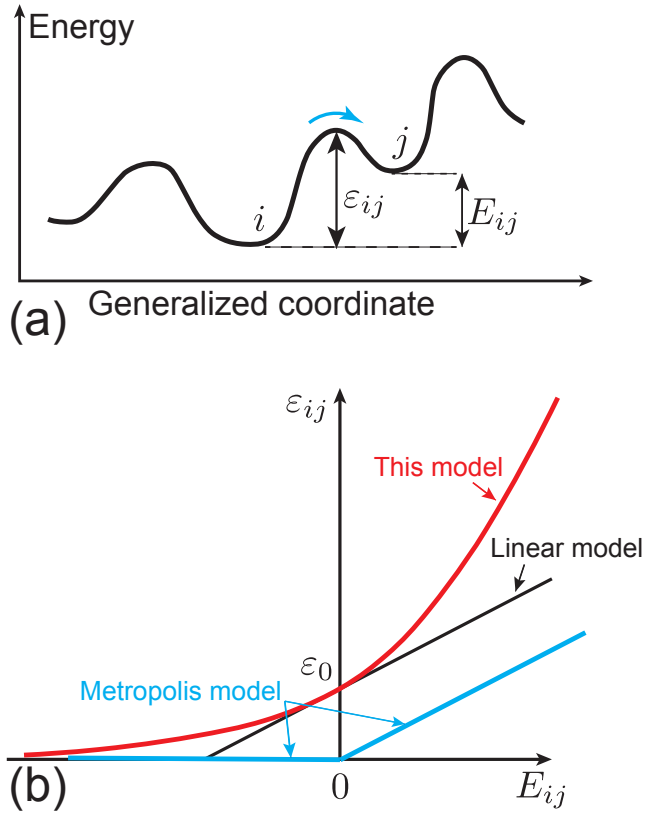


Figure 2: (a) Schematic 1D representation of energy landscape of a system jumping between energy minima by thermal fluctuations. ε_{ij} is the transition barrier from state i to state j with energies E_i and E_j , respectively. (b) The transition barrier as a function of energy difference $E_{ij} = E_j - E_i$ in the present model compared with the linear model (Eq.(11)) and the Metropolis model (Eq.(14)).

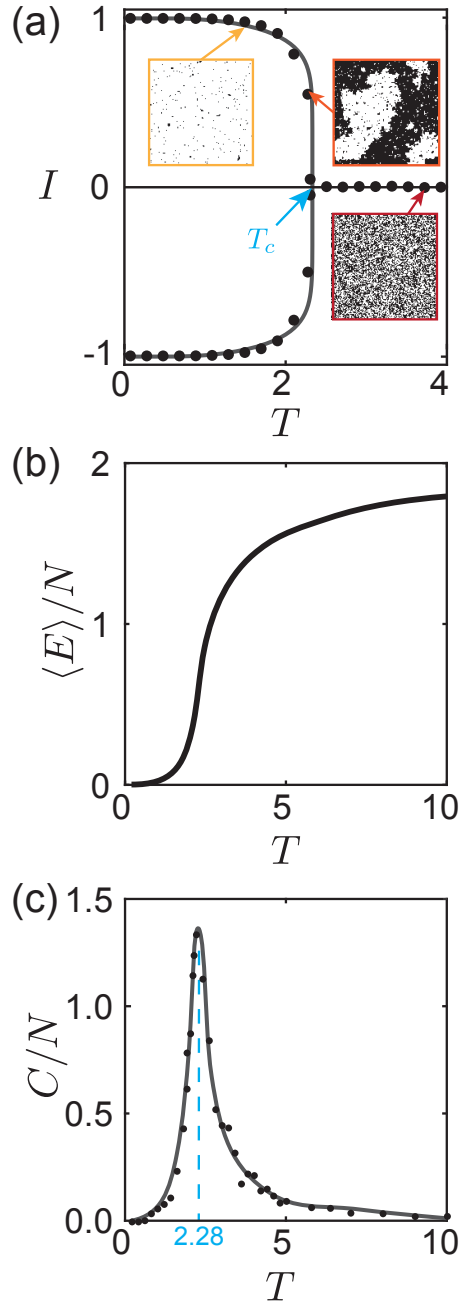


Figure 3: Properties of the solute-free system. (a) Average orientation (color) I as a function of temperature. The points were computed in this work and the lines represent the analytical solution (20). The insets show typical structures of single-crystalline states at low temperatures, near the critical point T_c , and the disordered state above T_c . (b) Energy per cell as a function of temperature. The curve has been smoothed for numerical differentiation. (c) Heat capacity per cell computed by Eqs.(17) (curve) and (18) (points). The peak at $T = 2.28$ marks the approximate location of the critical temperature T_c .

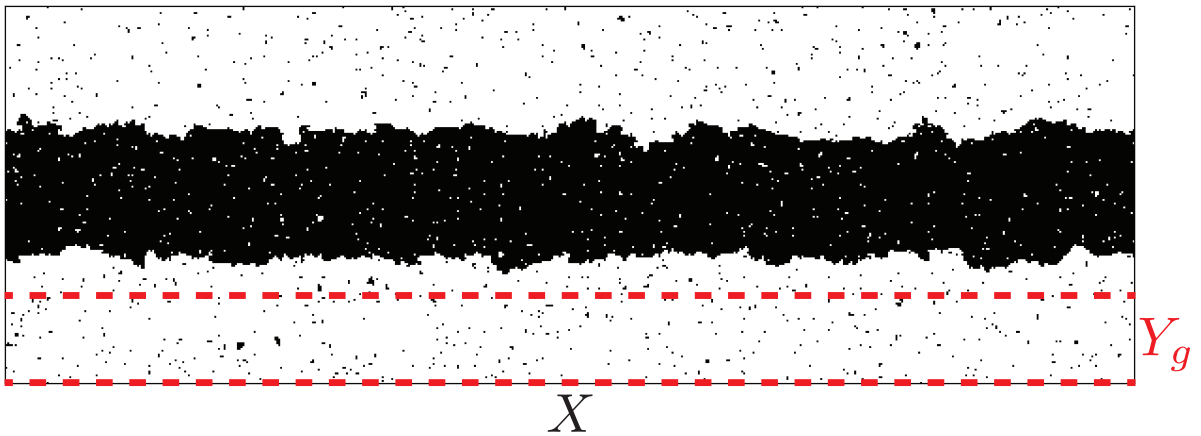


Figure 4: The excess GB energy calculations by Eq.(25). The dashed rectangle outlines a region with dimensions $X \times Y_g$ selected to represent the grain energy E_g .

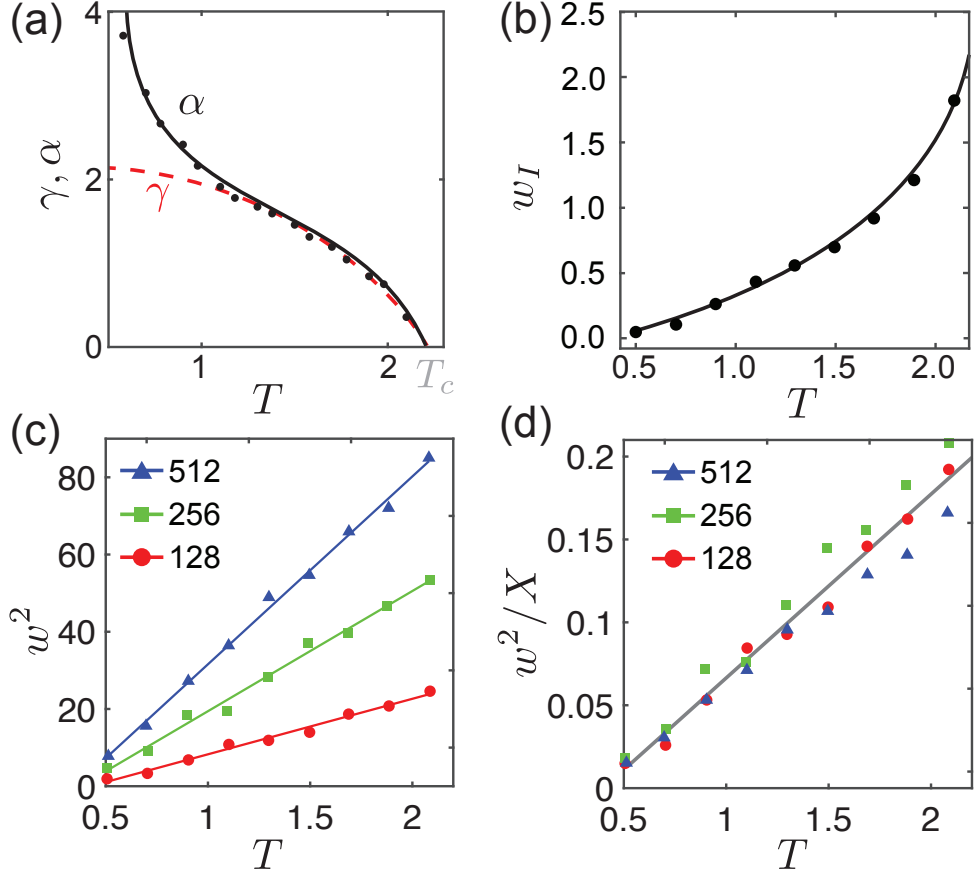


Figure 5: Solute-free GB properties as a function of temperature. (a) GB free energy γ and stiffness α . The points represent individual calculations of α by the capillary wave method, while the curve serves as a guide to the eye. (b) Intrinsic interface width w_I . (c) Mean-squared GB width w^2 for three system sizes X indicated in the key. (d) Normalized mean-squared interface width w^2/X for three system sizes X indicated in the key. The highest temperature shown on the plots is close to the bulk critical point T_c . The results were obtained by KMC simulations within the present model.

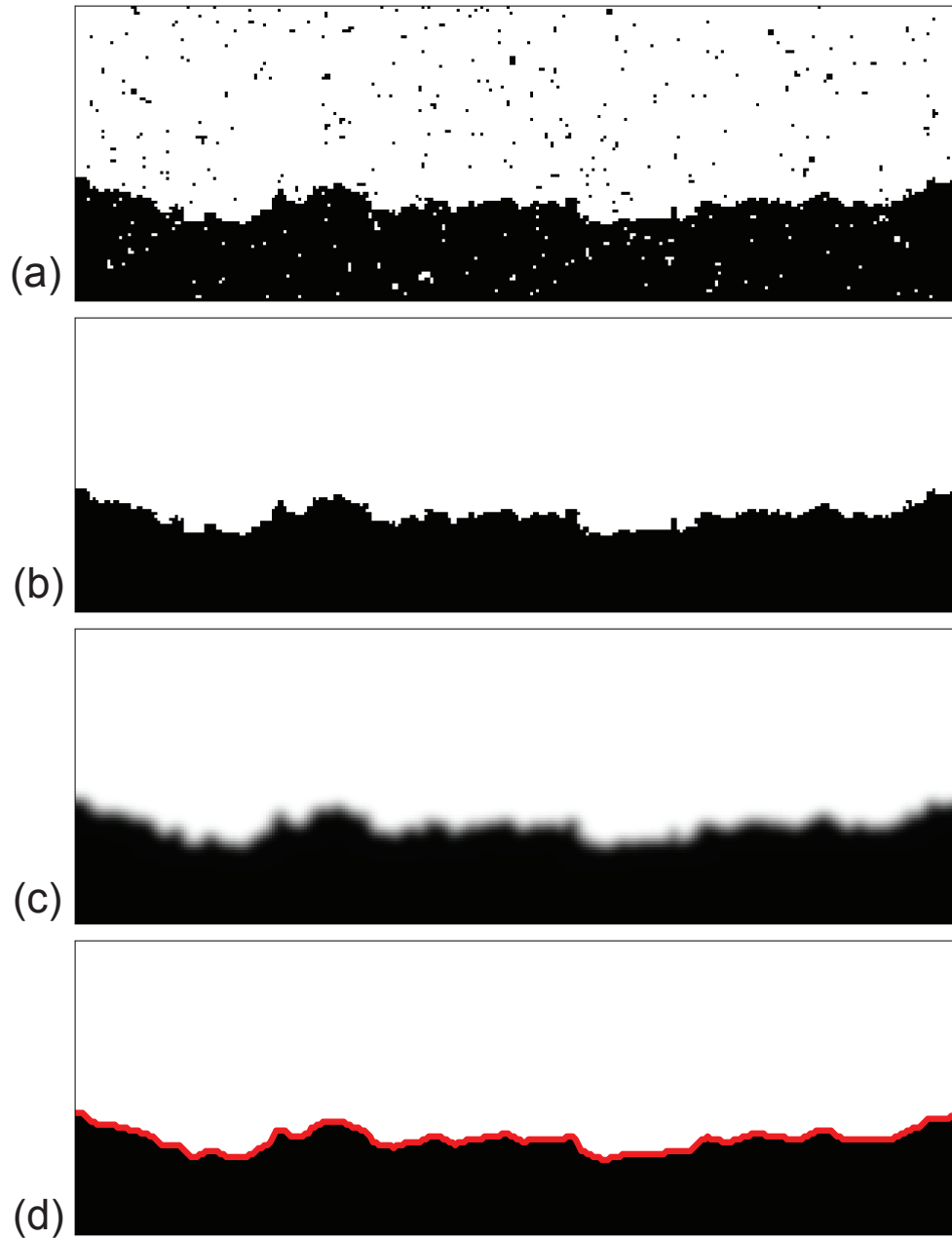


Figure 6: Example of GB shape calculation in the capillary fluctuation method. (a) Initial structure containing a fuzzy GB and background noise in the grains in the form of opposite-color cells. (b) The structure after removing the background noise in the grain. (c) GB shape smoothed by a Gaussian filter. (d) Final smoothed GB shape shown in red.

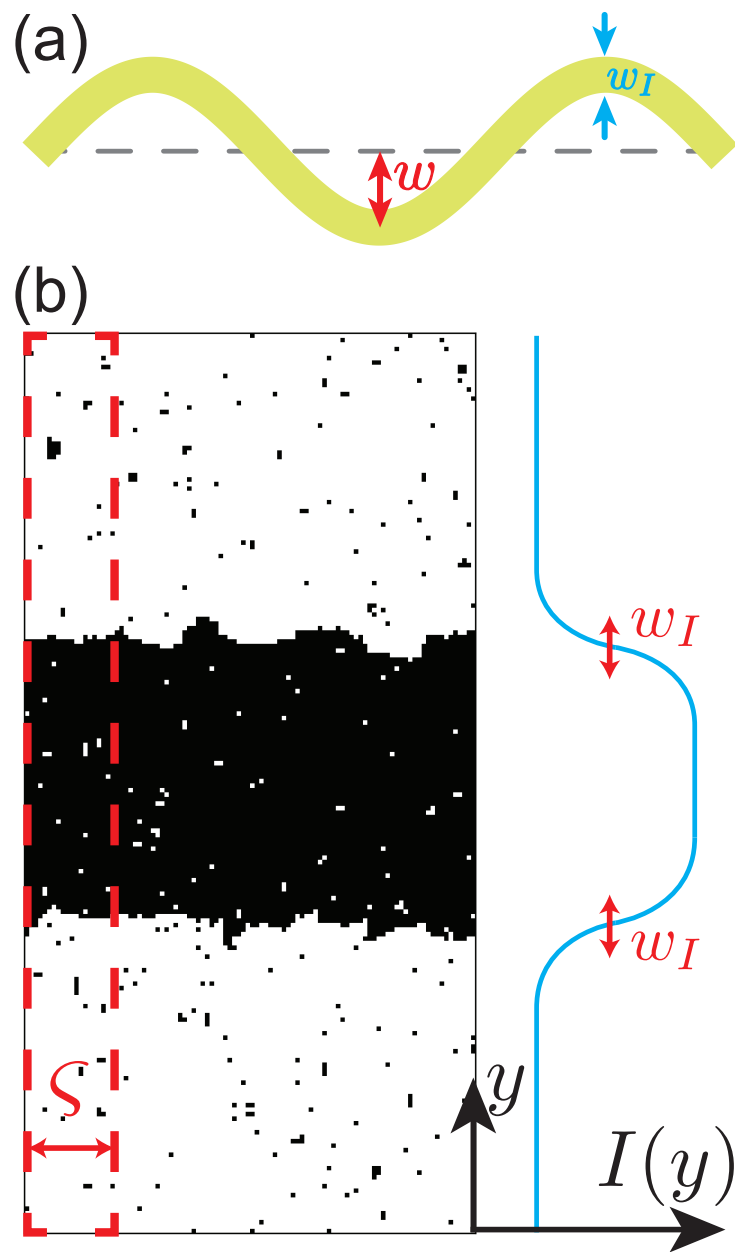


Figure 7: (a) Definition of the intrinsic GB width w_I and the mean-squared capillary width $\langle w^2 \rangle$. (b) Example of the w_I calculation. The dashed box indicates a stripe normal to the GB. The blue curves show the hyperbolic functions fitted to the color function $I(y)$ in the GB regions.

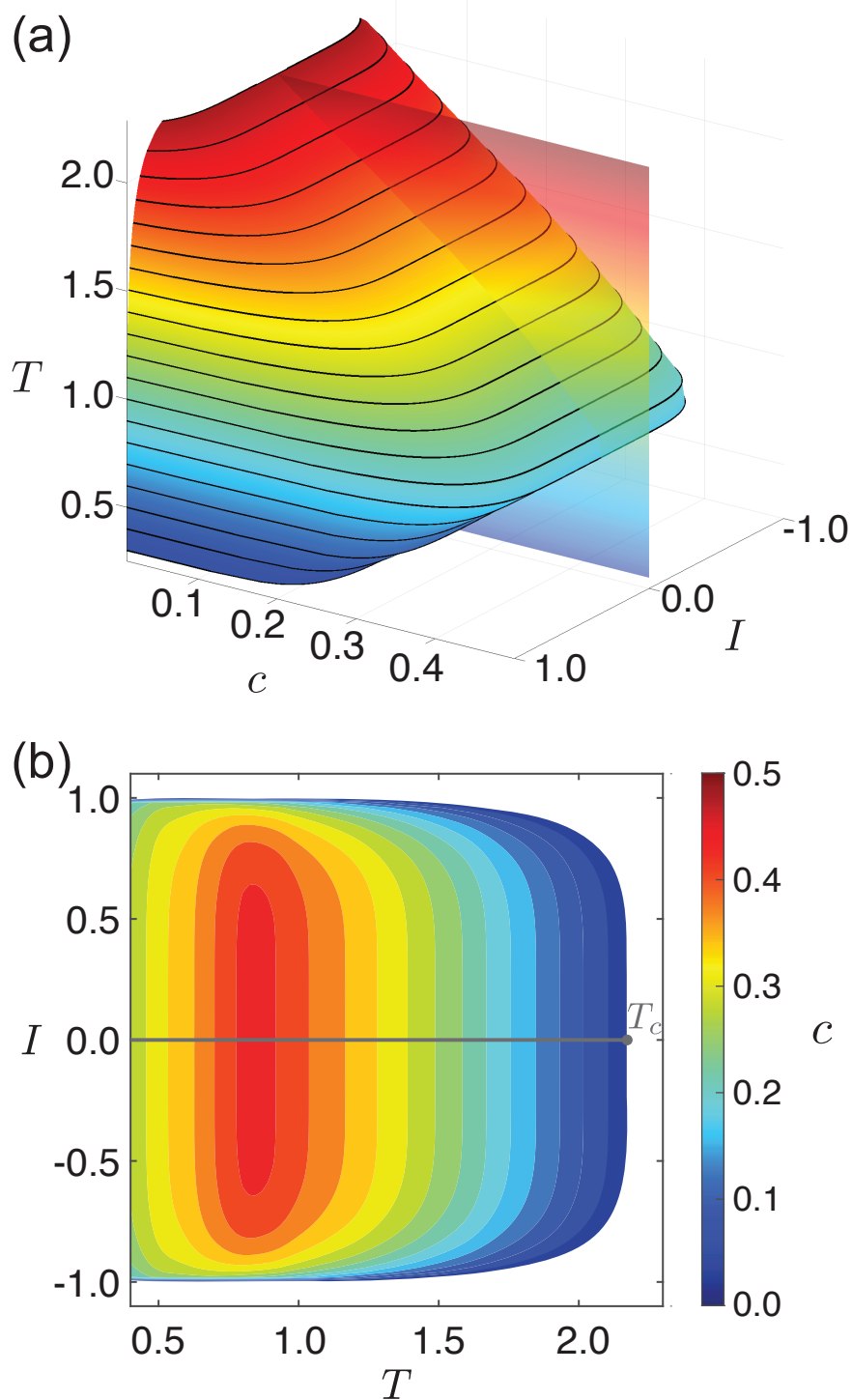


Figure 8: (a) Phase diagram in the composition-temperature-orientation coordinates. The segregation energy is fixed at $J_{sg} = 2$. (b) Slices of the phase diagram at different chemical compositions indicated in the color bar. Note that the iso-concentration contours form closed loops as the solute concentration increases. These loops indicate the existence of two critical points.

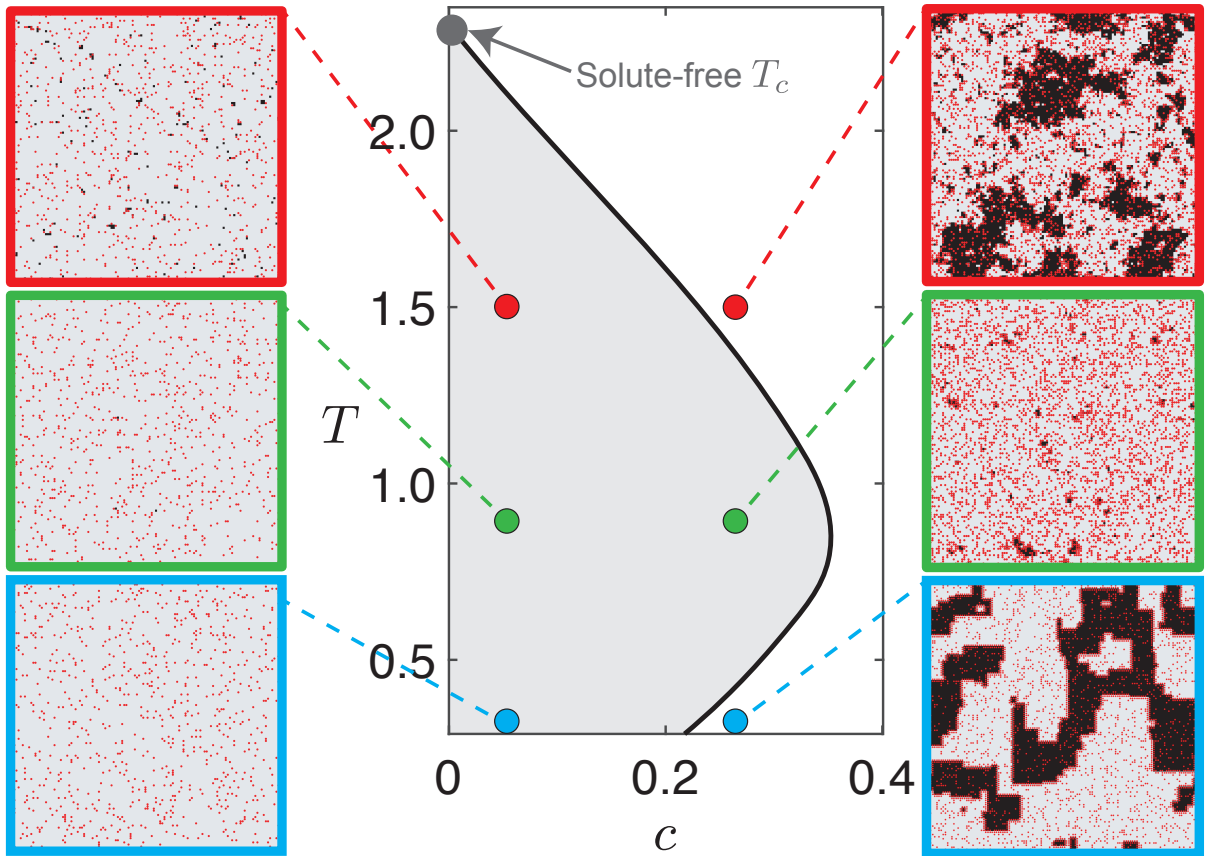


Figure 9: Temperature-composition phase diagram of alloys. The insets show representative structures at selected points on the diagram. The segregation energy is $J_{sg} = 2$. The red dots represent solute atoms.

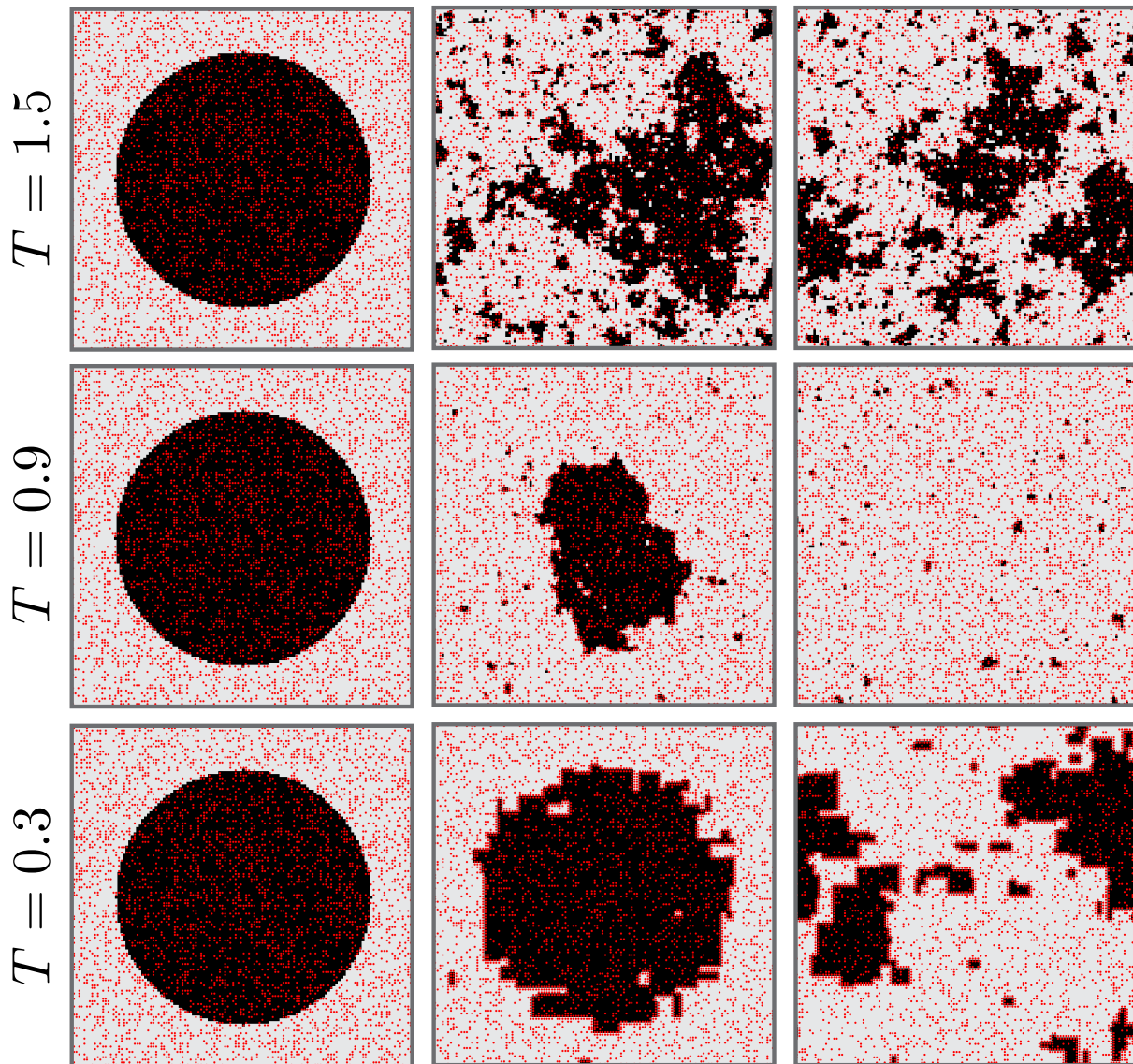


Figure 10: Single grain evolution in an alloy with $c = 0.25$ at three different temperatures. The left, middle, and right columns represent the initial, intermediate, and fully equilibrated structures, respectively. The results were obtained by KMC simulations with $J_{sg} = 2$.

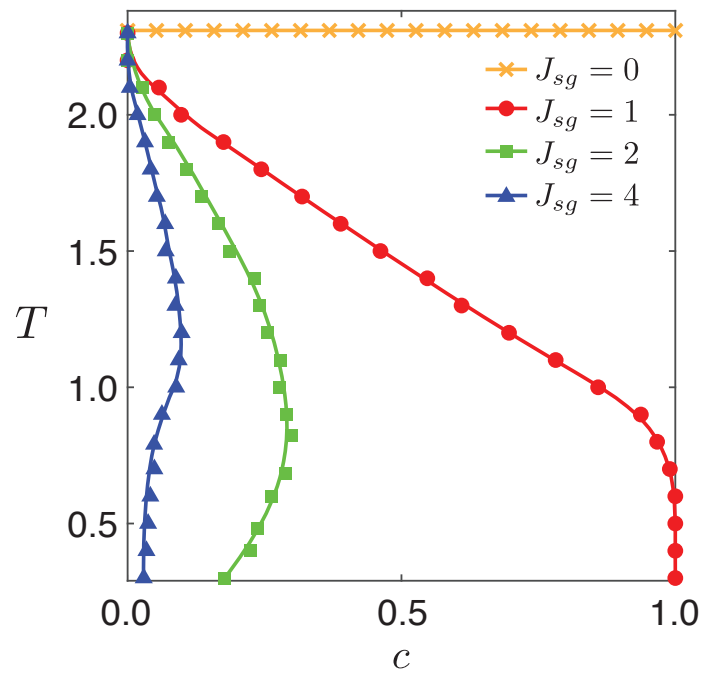


Figure 11: Temperature-composition phase diagrams for different choices of the segregation energy J_{sg} indicated in the key. The points represent individual simulations by the Metropolis Monte Carlo algorithm.

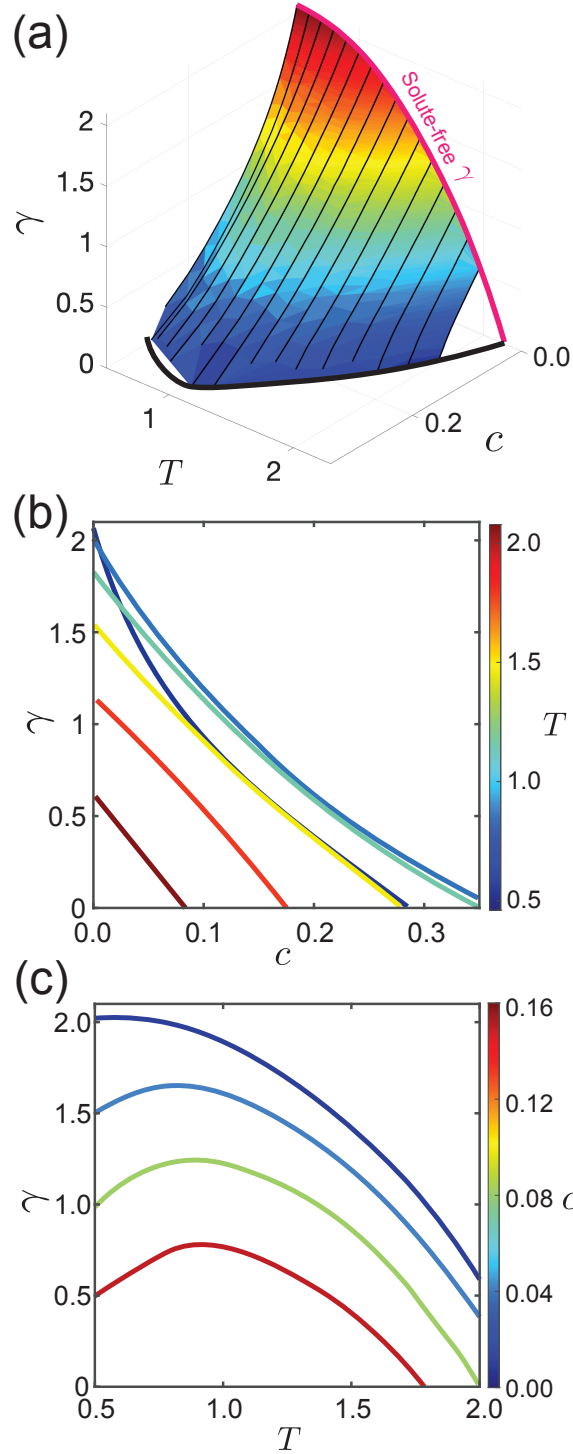


Figure 12: (a) Three-dimensional surface plot of GB free energy γ as a function of temperature T and solute concentration c . The red and black curves show the results for the solute-free system and the boundary of single-crystalline stability at which $\gamma = 0$. (b) Isothermal cross-sections of the surface in (a). (c) Iso-concentration cross-sections of the surface in (a). The segregation energy is $J_{sg} = 2$.

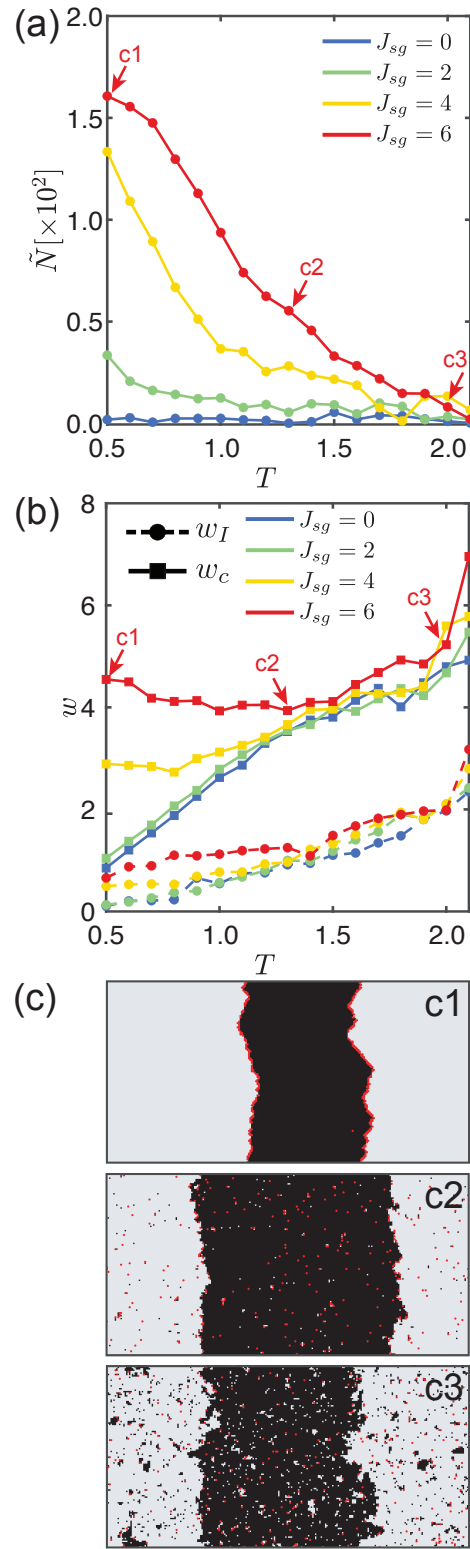


Figure 13: GB segregation \tilde{N} (a) and GB widths w_I and w_c (b) as a function of temperature for several J_{sg} values. The images in (c) show the structures at representative points c1, c2, and c3. The red dots represent solute atoms. The average solute concentration in the system is $c = 0.01$.

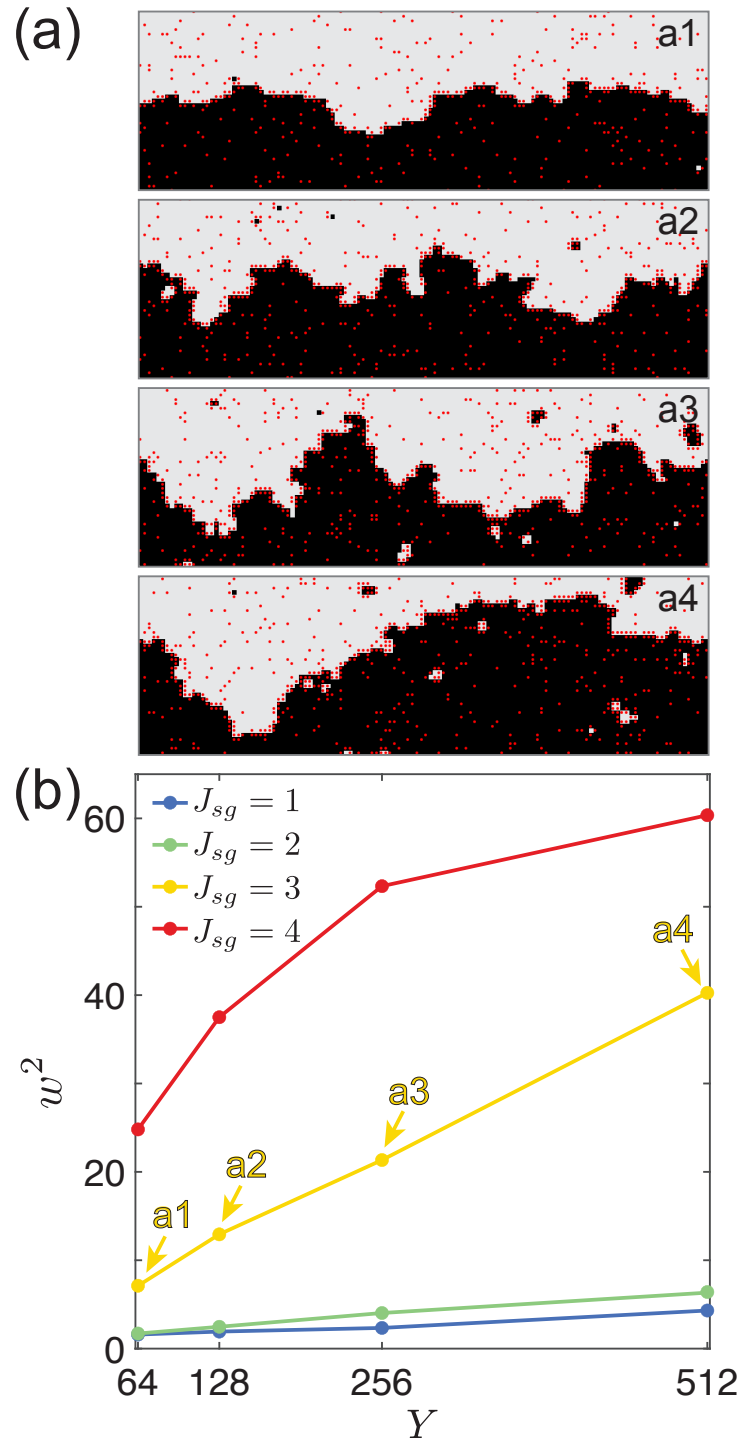


Figure 14: (a) Representative snapshots showing GB morphology for four system sizes Y . The red points represent solute atoms. The simulation temperature is $T = 0.7$, the average solute concentration is $c = 0.1$, and the GB segregation energy is $J_{sg} = 3$. (b) Capillary width as a function of system size for four values of J_{sg} .

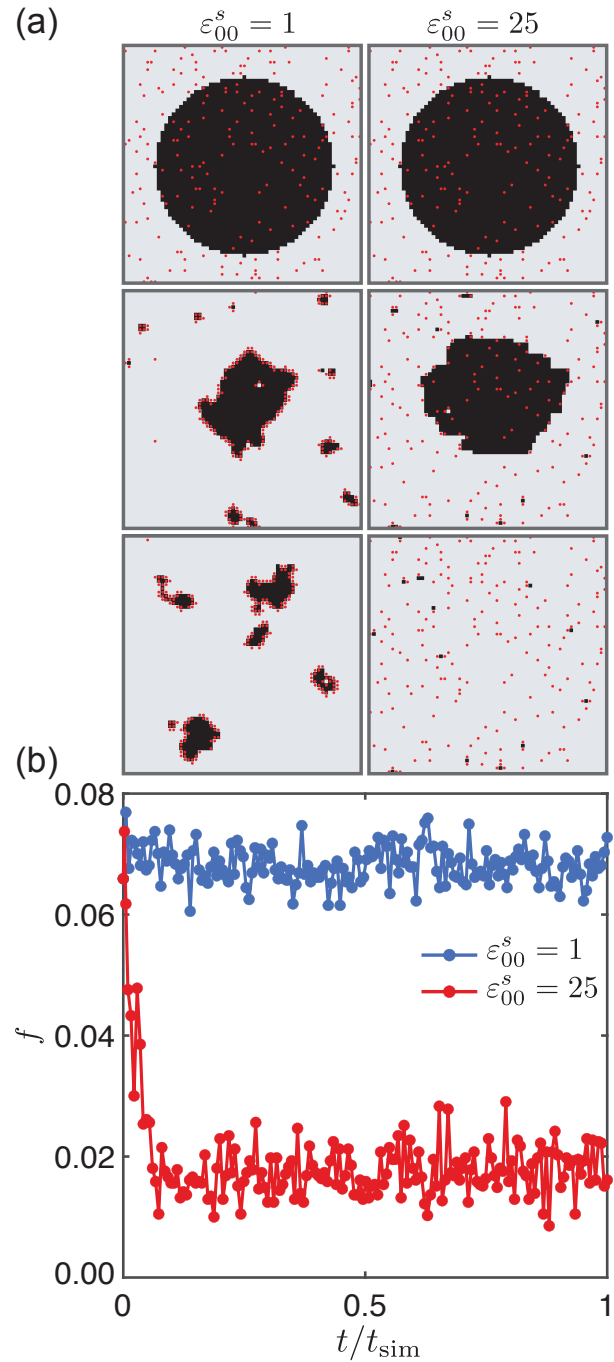


Figure 15: (a) Demonstration of the solute diffusivity effect on grain evolution. The circular grain with the initially random distribution of the solute (top row) evolves into different states (bottom row), depending on the solute diffusion rate. Left column: fast diffusion ($\varepsilon_{00}^s = 1$). The grain breaks into smaller grains and forms a stable polycrystal. Right column: slow diffusion ($\varepsilon_{00}^s = 25$). The grain shrink and disappears. (b) The fraction of GB sites f as a function of time t normalized to the total simulation time t_{sim} .

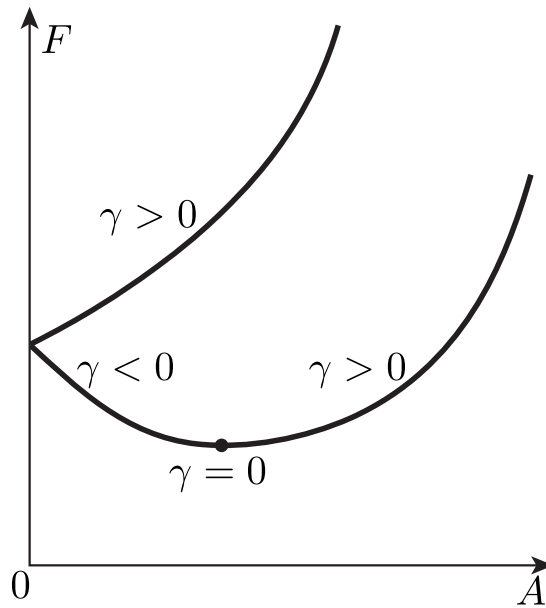


Figure 16: Schematic presentation of the free energy F as a function of grain boundary area A in a polycrystalline material. Upper curve: commonly observed increase of free energy with grain refinement when the GB free energy γ is positive. Lower curve: hypothetical decrease of free energy with grain refinement when $\gamma < 0$, followed by increase after γ changes sign. The point with $\gamma = 0$ represent a fully stable polycrystalline material.

SUPPLEMENTARY INFORMATION

A model of thermodynamic stabilization of nanocrystalline grain boundaries in alloy systems

Omar Hussein and Yuri Mishin

Department of Physics and Astronomy, MSN 3F3, George Mason University, Fairfax, Virginia 22030, USA

Grain boundary free energy in alloys from thermodynamic integration

In this supplementary file, we provide a more detailed description of the thermodynamic integration procedure applied in section 6 of the main text.

The grain boundary (GB) free energy in alloys was calculated in a periodic system comprising two parallel GBs (Fig. 1). The calculation is based on the two-dimensional form of the Gibbs adsorption equation

$$d(\gamma L) = -\tilde{N}d\mu, \quad T = \text{const.} \quad (1)$$

Here, γ is the GB free energy, L is the GB length, μ is the chemical potential of the solute atoms, and \tilde{N} is the total amount of solute segregation per GB. The latter is defined by the equation:

$$\tilde{N} = (c - c_g) \frac{N}{2}, \quad (2)$$

where c_g is the solute concentration in grain regions unaffected by the GBs, N is the number of cells in the system, and c is the average solute concentration in the alloy. The factor of two accounts for the presence of two GBs.

By integrating Eq.(1), we derive the following expression for the GB energy as a function of temperature and chemical potential:

$$\gamma(T, \mu) = \frac{1}{L(T, \mu)} \left[\gamma(T, \mu_*) L(T, \mu_*) - \int_{\mu_*}^{\mu} \tilde{N}(T, \mu') d\mu' \right]. \quad (3)$$

The asterisk denotes the chemical potential in the reference state (T, μ_*) . The ensemble-averaged GB length L can differ from the system size X due to capillary fluctuations. The reference chemical potential μ_* is chosen to achieve the smallest possible solute concentration at which \tilde{N} can still be reliably extracted from the simulations. The solute-free $\gamma(T)$ values were calculated in section 4.2. Metropolis Monte Carlo simulations were performed on a 128×256 system with temperatures between 0.3 and 2.0. To ensure that the system has reached thermodynamic equilibrium and collect sufficient statistics, the simulations comprised about 10^9 Monte Carlo steps.

The integration in Eq. (3) requires several ingredients, which were obtained as follows. First, we extracted the GB shapes from the simulation snapshots. The challenge in doing so is caused by the fuzziness of the GBs and the background noise in the grains. The noise in the gains is caused by the numerous cells of opposite color, either isolated or aggregated into small clusters. This noise is especially significant at high temperatures. An example is shown in Fig. 1(a). An algorithm was developed to identify the “wrong” color cells/clusters lying inside the grains and reverse their color to that of the grain (Fig. 1(b)). This grain-cleaning procedure was applied to all snapshots saved during the simulations. Next, the GBs were identified and the instantaneous average GB positions \bar{y} were calculated:

$$\bar{y} = \frac{1}{X} \sum_{n=1}^X y_n, \quad (4)$$

where y_n are the y -coordinates of the GB cells (the y -axis is normal to the GBs). The instantaneous positions of the two GBs were monitored during the simulations, allowing us to choose regions containing the GBs and regions located entirely inside the grains. For example, Fig. 1(b,c) shows such regions outlined by the dashed red and blue lines, respectively. The grain regions were used to compute the solute concentration in the grains, c_g , required for computing \tilde{N} by Eq. (2). Another required quantity is the average solute concentration in the system, c , which was found by simply counting the solute atoms.

The next ingredient, the GB length L , was calculated as follows:

$$L = \left\langle \frac{1}{4} \sum_k \lambda_k \right\rangle, \quad \text{where } \lambda_k = \begin{cases} 1 & \text{if } n_k \neq 0, \\ 0 & \text{if } n_k = 0. \end{cases} \quad (5)$$

Here, the angular brackets indicate ensemble averaging, and the factor of 1/4 eliminates the double-counting of pairs of GB cells and accounts for the presence of two GBs in the system. As an example, Fig. 1(d) shows a zoom-in view of one of the GBs with GB cells color-coded by the variable n_k .

The described calculations of c , \tilde{N} , and L were repeated for a set of chemical potentials and temperatures. Fig. 2(a,b) shows c and \tilde{N} as a function of μ for four representative

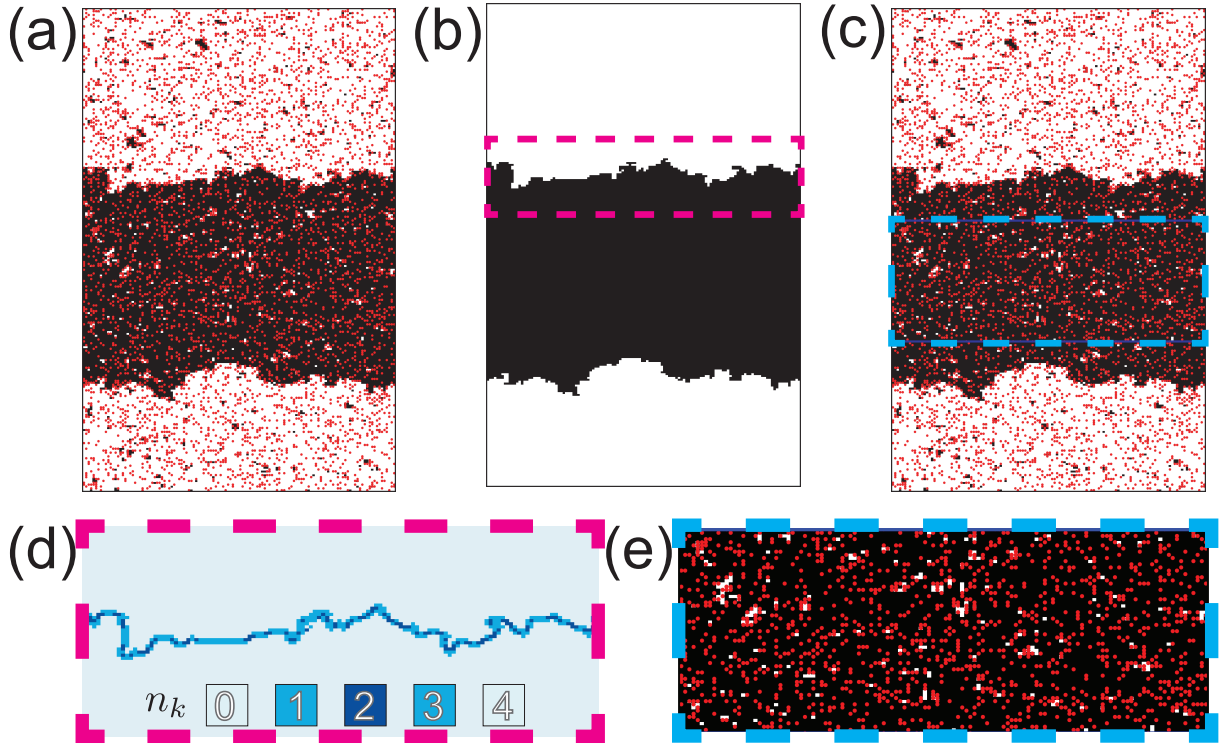


Figure 1: Example of GB shape analysis for thermodynamic integration of the GB free energy in alloys. (a) Initial structure containing a fuzzy GB and background noise in the grains. (b) “Clean” structure after removing the noise in the grains. The dashed red lines outline a box containing a GB. (c) The box bounded by the dashed blue lines represents GB interiors and is used for computing the solute concentration in the grains (c_g). This box is shown separately in (e). (d) The GB portion inside the dashed red box in (b). The GB cells are color-coded by the values of the parameter n_k (the tracker of GB cells). Such GB structures were used to compute the GB length L .

temperatures. The reference chemical potential was chosen to be $\mu_* = -10$. The numerical integration in Eq.(3) was performed using a quadratic spline interpolation of \tilde{N} as a function of μ , resulting in continuous curves shown in Fig. 2(c). While Eq.(3) yields the function $\gamma(T, \mu)$, the more convenient function $\gamma(T, c)$ was obtained from the plots of c versus μ exemplified in Fig. 2(a).

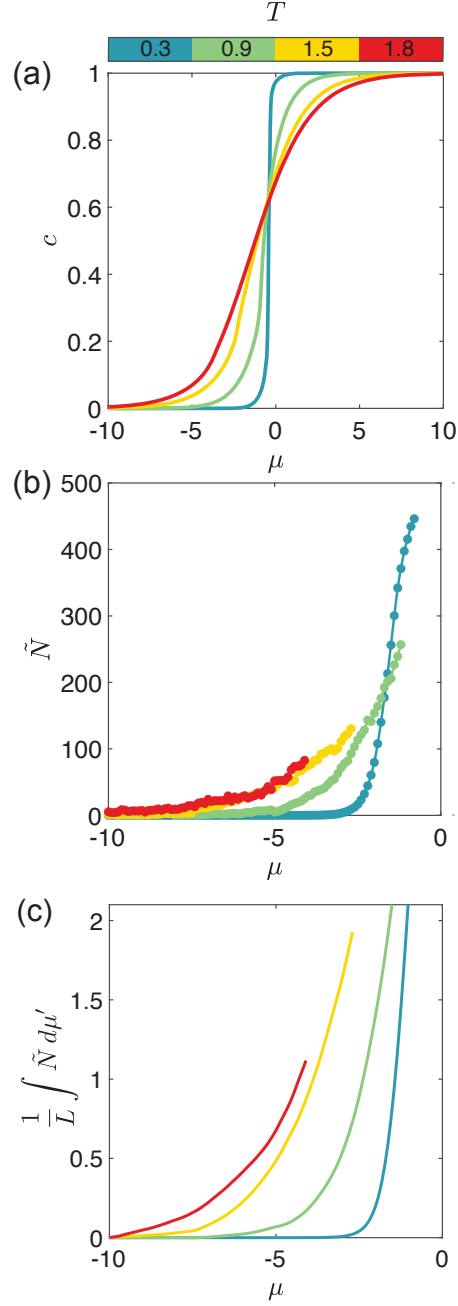


Figure 2: Steps of the GB free energy calculation in alloys at the temperatures of 0.3, 0.9, 1.5, and 1.8. by thermodynamic integration. (a) The relationship between the alloy concentration c and the chemical potential μ . (b) The total amount of GB segregation \tilde{N} as a function of chemical potential μ . The data points represent individual simulations. The curves were obtained by quadratic spline interpolation. Each curve starts and ends at critical points where the bicrystalline structure disintegrates. (c) The integral in Eq.(3) as a function of μ . The integration was performed using the quadratic spline interpolation of the function $\tilde{N}(\mu)$.